Lithos 190–191 (2014) 292–312

Contents lists available at ScienceDirect

Lithos

journal homepage: www.elsevier.com/locate/lithos

Metamorphic *P–T* conditions across the Chugach Metamorphic Complex (Alaska)—A record of focussed exhumation during transpression

Emilie Bruand [a,b,*], Deta Gasser [a,c], Kurt Stüwe [a]

[a] Department of Earth Sciences, Karl-Franzens Universität, Universitätsplatz 2, 8010 Graz, Austria
[b] School of Earth and Environmental Sciences, Portsmouth University, Burnaby building, Burnaby Road, Portsmouth PO1 3QL, United Kingdom
[c] Geological Survey of Norway, Postboks 6315 Sluppen, 7491 Trondheim, Norway

ARTICLE INFO

Article history:
Received 30 April 2013
Accepted 11 December 2013
Available online 19 December 2013

Keywords:
Chugach terrane (Alaska)
Accretionary prism
Thermobarometry
Migmatite
Exhumation process
Ridge subduction

ABSTRACT

The Chugach Metamorphic Complex (CMC) is a large high-grade metamorphic complex that developed in the Eocene within the Chugach accretionary complex along the margin of Alaska where subduction is still ongoing. The CMC has a conspicuous asymmetric structure with a migmatitic zone flanked in the north and west by amphibolite facies schists and in the south by a metabasite belt. To the north and south, major, crustal-scale fault zones juxtapose the Chugach terrane against much lower-grade and less-deformed sequences belonging to different terranes. Curiously these crustal-scale structures are known to have largely strike slip motion posing the question as to the nature of the exhumation of the high-grade complex between them. However, *P–T* conditions which would allow an estimation of the amount of exhumation were lacking for large parts of the complex. This paper presents petrographic descriptions, biotite–garnet thermometry, RSCM thermometry, average *P–T* calculations and pseudosection modelling from three major across-strike transects covering the complex from west to south-east. Our results reveal that, both temperature and pressure vary substantially across the complex. More specifically, peak metamorphic conditions evolve from 4–7 kbar and ~550–650 °C in the northern schist zone to 5–11 kbar and ~650–750 °C in the migmatite zone in the south of the complex. The higher pressure estimates in the south of the complex indicate that focussed exhumation must have occurred in this area and was probably initiated by the subduction of a high topographic relief (intra-oceanic arc or ridge subduction) and the accretion of the metabasite belt in the south. Exhumation of the CMC occurred in an overall transpressive strain regime, with strike-slip deformation concentrated along the northern Border Range fault zone and thrusting and exhumation focussed within the southern migmatite zone and splay faults of the Contact fault zone. The *T*/*P* ratios in the southern migmatite zone indicate that the thermal perturbation of the migmatites is less than previously inferred. These new results, associated with the structural data and the accretion of a metabasite belt in the south of the complex, seem incompatible with the existing ridge-subduction models.

1. Introduction

Long, narrow belts of high grade metamorphic rocks, exhumed within an overall convergent plate tectonic setting, occur all around the world and are often referred to as metamorphic wedges. One of the best-known examples for such a metamorphic wedge is the Crystalline Complex of the Central Himalayas (e.g. Hodges, 2006; Yin, 2006). The exhumation of such belts has been variably explained by: (i) rigid extrusion of the high grade belt between shear zones bounding it on either side (e.g. Hodges et al., 1993, 1996), (ii) channel flow (e.g. Cloos, 1982; Grujic et al., 2002; Harris, 2007), (iii) general shear extrusion (e.g. Northrup, 1996; Vannay and Grasemann, 2001), or (iv) buoyancy assisted by erosion and tectonic processes (e.g. Chemenda et al., 1995). Two kinds of high-grade wedges can be found in mountain belts: (i) (U)HP–LT wedges resulting from the exhumation of subducted material and (ii) HT wedges resulting from the exhumation of products linked to continental collision (e.g. shear heating, thickening of crust, and fluid flow). It is extremely uncommon to find a HT metamorphic belt developing within an accretionary prism while subduction is still ongoing (e.g. Ryoke belt; Brown, 1998a, 1998b, 2002). One such exceptional example is the Chugach Metamorphic Complex (CMC) of southern Alaska (Fig. 1; Gasser et al., 2011, 2012a; Hudson and Plafker 1982; Hudson and Plakfer et al., 1982; Pavlis and Sisson, 1995; Scharman and Pavlis, 2012; Scharman et al., 2011, 2012; Sisson et al., 1989). This upper amphibolite facies metamorphic complex developed during the Eocene within the accretionary prism of the Chugach terrane, which formed in response to subduction of on oceanic plate beneath the North American continent (Fig. 1; e.g. Plafker et al., 1994). The CMC has a peculiar geometry reminiscent of an extrusion wedge. It consists of a ~350 km long and 5–20 km wide upper amphibolite facies migmatitic zone, which in its western and northern parts is surrounded by lower amphibolite facies schists, which in turn are surrounded by greenschist

* Corresponding author at: School of Earth and Environmental Sciences, Portsmouth University, Burnaby building, Burnaby Road, Portsmouth PO1 3QL, United Kingdom.
E-mail address: emilie.bruand@port.ac.uk (E. Bruand).

0024-4937/$ – see front matter © 2013 Elsevier B.V. All rights reserved.
http://dx.doi.org/10.1016/j.lithos.2013.12.007

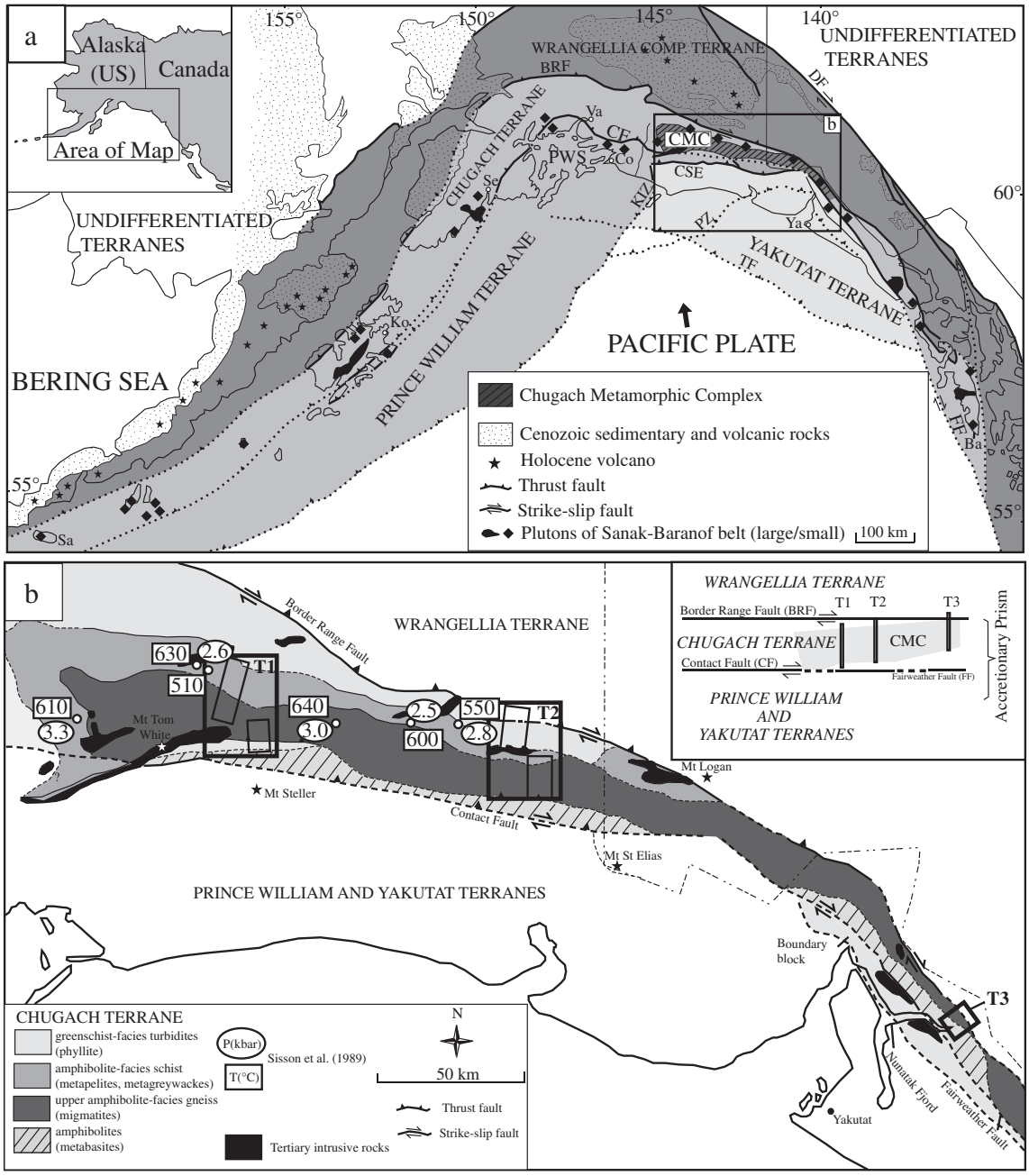

Fig. 1. Geological map of the Chugach Metamorphic Complex (CMC). (a) Tectonic overview of the southern Alaskan margin with terrane names and plutons of the Sanak–Baranof belt (modified after Gasser et al., 2011). Sa = Sanak, Ko = Kodiak, Se = Seward, PWS = Prince William Sound, Va = Valdez, Co = Cordova, Ya = Yakutat, Ba = Baranof Island, BRF = Border Range Fault, CF = Contact Fault, KIZ = Kayak Island Zone, CSE = Chugach-St-Elias-Fault, PZ = Pamplona Zone, TF = Transition Fault, FF = Fairweather Fault, DF = Denali Fault. (b) Geological map of the Chugach Metamorphic Complex and surrounding terranes (modified after Gasser et al., 2011; Sisson et al., 1989). T1, T2 and T3 refer to transects 1, 2 and 3 as described the text. Previously obtained *P–T* data are indicated (from Sisson et al., 1989).

facies phyllites (Fig. 1). Available *P–T* data are restricted to the western and northern parts of the complex where Sisson et al. (1989) derived 550 °C–650 °C and 2–3 kbar (Fig. 1b). These data indicate elevated temperatures at low pressures, suggesting that only limited exhumation of rocks occurred, and that a thermal anomaly relative to a normal subduction zone temperature gradient is required. Therefore, the development of this metamorphic complex has been mainly ascribed to either: the subduction of a spreading ridge (e.g. Bradley et al., 2003; Haeussler et al., 2003; Pavlis and Sisson;, 1995; Scharman and Pavlis, 2012; Scharman et al., 2012; Sisson and Pavlis, 1993) or the subduction of a transform fault (Sisson et al., 2003). However, the occurrence of the intensely deformed, high grade metamorphic rocks of the CMC in between less-deformed and lower-grade rocks within the accretionary prism illustrates that focussed exhumation must have taken place at least locally within the Chugach and Prince William terranes (e.g. Gasser et al., 2011). A detailed investigation of the metamorphic grade changes across and along-strike of the complex, which would allow a discussion of the exhumation mechanisms and the heat sources for this complex, is lacking so far and is the main focus of this work.

We present a detailed petrological study from three across-strike transects covering the CMC from west to south-east along-strike. Petrological analysis, garnet–biotite thermometry, average *P–T* calculations, Raman spectroscopy on carbonaceous material (RSCM) geothermometer, and thermodynamic modelling (THERMOCALC) are used

together with structural and geochronological data (Gasser et al., 2011, 2012a) to discuss the exhumation mechanisms and implications for heat sources for this complex.

2. Geological setting

The geology of the southern margin of Alaska between Sanak Island in the west and Yakutat in the east is currently dominated by the subduction of the Pacific plate beneath the North American continent (Fig. 1). Southeast of Yakutat, the Pacific–North American boundary is dominated by strike-slip tectonics along the Queen Charlotte-Fairweather fault system. The subduction system in southern Alaska has operated intermittently at least since the Jurassic and has accreted a series of terranes and accretionary prisms to the continent, reflecting the successive convergence. From north to south these major units are known as the composite Paleozoic to Mesozoic Wrangellia terrane, the Cretaceous to Paleogene Chugach and Prince William terranes and the Mesozoic to Cenozoic Yakutat terrane (Fig. 1; e.g. Plafker et al., 1994).

The Chugach terrane hosts the Chugach Metamorphic Complex and, together with the adjacent Prince William terrane, represents a ~2200 km long accretionary prism with a maximum width of ~100 km (Fig. 1). To the north, it is juxtaposed against the Wrangellia composite terrane along the Border Range Fault System (Fig. 1, e.g. Pavlis and Roeske, 2007; Plafker et al., 1994). To the south, the Yakutat terrane is colliding with the accretionary prism along the Chugach St. Elias Fault and the Fairweather Fault System (Fig. 1; e.g. Bruhn et al., 2004). In the eastern part of the Gulf of Alaska, the Contact Fault System separates the accretionary prism into the northern Chugach and the southern Prince William terranes (Fig. 1; e.g. Bol and Roeske, 1993). The accretionary prism consists of a sequence of flysch sediments which are regionally metamorphosed at zeolite to greenschist facies conditions (e.g. Dusel-Bacon, 1994). Within the CMC, these flysch sediments are metamorphosed to upper amphibolite facies conditions (e.g. Hudson and Plafker, 1982; Hudson et al., 1977; Sisson et al., 1989).

The Chugach and Prince William terranes are intruded by the Sanak–Baranof plutonic belt (Fig. 1, e.g. Farris and Paterson, 2009; Hudson et al., 1979). The age of the plutons in this belt decreases from west to east from 61 to 50 Ma (e.g. Bradley et al., 1993, 2003). This age trend, the forearc position and the geochemistry of the granitoids have been explained by subduction of a mid-oceanic spreading ridge (e.g. Bradley et al., 1993, 2003; Haeussler et al., 2003; Marshak and Karig, 1977; Pavlis and Sisson, 1995). This ridge subduction event is also widely accepted to be responsible for the HT–LP metamorphism of the Chugach Metamorphic Complex (e.g. Bradley et al., 2003; Haeussler et al., 2003; Pavlis and Sisson, 1995; Scharman et al., 2012; Sisson and Pavlis, 1993).

The Chugach Metamorphic Complex itself is mainly developed inside the accretionary prism of the Chugach terrane and is defined as the region that substantially exceeds the regional background metamorphic grade of lower greenschist facies (e.g. Hudson and Plafker, 1982). The Complex is made of amphibolite facies schists in the north and west and migmatitic gneisses in the south. Within the northern schist zone and western gneiss zone, the wide-spread occurrence of andalusite and sillimanite is interpreted to reflect low-pressure high-temperature peak metamorphic conditions in these areas (e.g. Pavlis and Sisson, 1995; Sisson and Pavlis, 1993); Sisson et al. (1989) derived *P–T* conditions of 2–3 kbar and 550–650 °C at several localities (Fig. 1b). To the south of the migmatitic gneisses, a narrow belt of metabasite of similar metamorphic grade is tectonically juxtaposed in a complex manner along the Contact Fault System in the west and the Fairweather Fault System in the east against the much lower grade Prince William and Yakutat terranes rocks further south (Fig. 1; Bruand et al., 2011; Gasser et al., 2011; Lull and Plafker, 1990).

The CMC is composed of four main rock types. The majority of the complex consists of (1) metapelitic to calcareous metapelitic rocks, which are interlayered with (2) less aluminous metagraywackes with frequent pods of calcsilicates (e.g. Hudson and Plafker, 1982); (3) metabasites occur as rare layers intercalated with the aforementioned rocks and as a large, coherent belt along the southern boundary of the CMC (Bruand et al., 2011; Lull and Plafker, 1990); and (4) granitoid rocks of the Sanak–Baranof belt occur frequently on all scales (Harris et al., 1996; Pavlis and Sisson, 1995; Sisson et al., 1989). The metasedimentary and the metavolcanic rocks are deformed by three ductile deformation phases. D_1 is associated with the accretion of the sediments and is inferred to have formed at around 60–55 Ma (Gasser et al., 2011; Pavlis and Sisson, 1995; Scharman et al., 2011). This fabric is largely overprinted by a pervasive flat lying S_2 fabric of the second ductile deformation phase which is in turn overprinted by a steep S_3 fabric, which is most prominently developed in the migmatitic core of the complex (Gasser et al., 2011; Pavlis and Sisson, 1995; Scharman et al., 2011). Both S_2 and S_3 developed during a short time interval around 55–51 Ma, coeval with peak metamorphic conditions (Gasser et al., 2011, 2012a, 2012b). Peak metamorphism was followed by rapid cooling west of the Canadian border shortly after 50 Ma, and slow cooling south of the Canadian border (Gasser et al., 2011; Sisson et al., 1989). Final cooling and exhumation occurred in connection with the Yakutat collision after about 15 Ma (Enkelmann et al., 2008; Gasser et al., 2011).

3. Investigated transects

In order to obtain *P–T* conditions representative for the complex, three N–S transects crossing the different metamorphic zones of the CMC have been studied (Figs. 1b, 2). The geology and structure of these transects are described in more detail in Gasser et al. (2011), but a short summary of the most relevant structures needed for the interpretation of *P–T* results is presented below.

In transect 1, the phyllite zone is characterised by a south-dipping pressure solution foliation (S_1), the schist zone by a flat-lying biotite-foliation (S_2) which is crenulated by S_3, and the gneiss zone by the subvertical S_3 foliation (Fig. 2a; Gasser et al., 2011). Fold axes and stretching lineations in all these domains are mainly subhorizontal east–west trending (Fig. 2a). However, in the southernmost gneiss zone, the stretching lineation associated with S_3 becomes progressively steeper, and younger, retrograde chlorite- and muscovite-bearing shear zones contain N-plunging lineations (Fig. 2a; Gasser et al., 2011). These shear zones are interpreted to be part of a larger fault system which runs below a glacier, and which separates the migmatitic gneisses from lower-grade phyllites in the south (Fig. 2a).

In transect 2, the phyllite and schist zones are characterised by the south-dipping S_1 foliation with subhorizontal stretching lineations, whereas the gneiss zone exhibits a fan-shaped geometry with the S_3 foliation plunging south in the northern part and north in the southern part (Fig. 2b). The stretching lineations on S_3 become progressively steeper towards the south, and several ductile to semi-brittle muscovite- and chlorite-bearing shear zones show N-plunging stretching lineations with north-side-up sense of movement indicated by asymmetric clasts and folds (Fig. 2b; Gasser et al., 2011). These shear zones juxtapose the migmatitic gneisses against the metabasite belt in the south (Fig. 2b). Transect 3 is characterised by the subvertical S_3 foliation with NW-plunging lineations in the southwestern part and southeast-plunging lineations in the northeastern part (Fig. 2c; Gasser et al., 2011).

4. Petrography

In this study, attention is focussed on metapelites as the main lithology of the CMC. In transects 1 and 3, Ca-rich metapelites dominate (e.g. samples B23, B26; Table 1, Gasser et al., 2012b), while in transect 2 most rocks have typical metapelitic compositions and Ca-rich compositions are rare. The petrological descriptions are given according to metamorphic grade, and follow the subdivision of

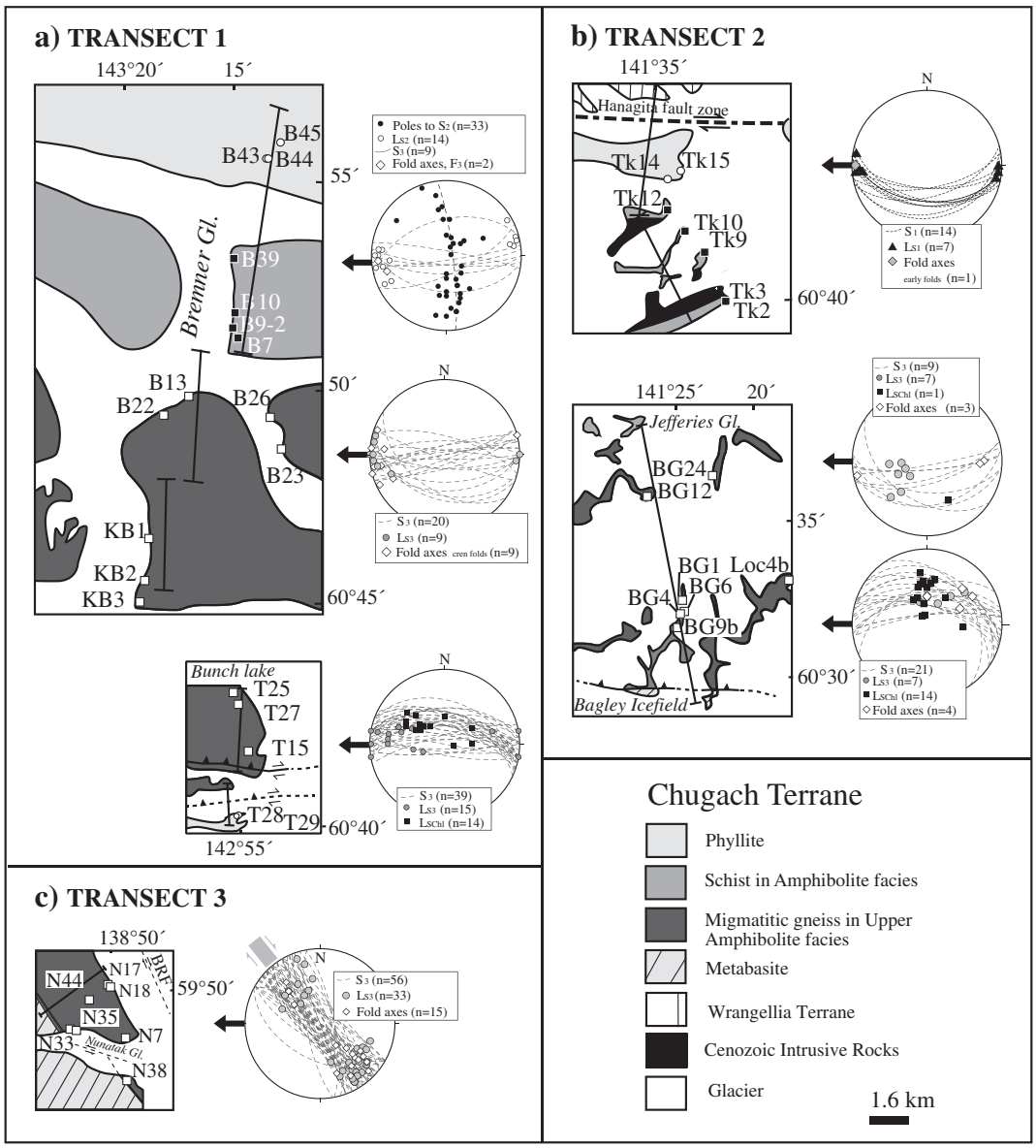

Fig. 2. Geological sketch maps of the three different transects. The location of the transects are indicated in Fig. 1b. Sample locations of this study are shown with different symbols according to the metamorphic grade of the rocks (circle = phyllite, black square = schist, white square = migmatite). Black lines correspond to cross-sections in Figs. 6 and 8. (a) Transect 1: maps of the Bremner glacier region, (b) Transect 2: maps of the region between the Hanagita fault and the Bagley Icefield and (c) Transect 3: Map of the Nunatak Glacier region. The main structural features relevant for the petrological evolution of the complex are shown in stereoplots (lower hemisphere equal area projections). Note the plunging to subvertical orientation of stretching lineations in the southern parts of transects 1 and 2, in contrast to the subhorizontal stretching lineations in the northern parts. The data are compiled from Gasser et al. (2011). Abbreviations in stereoplots: chl = chlorite, cr = crenulations, Ls = stretching lineation, S = foliation.

Hudson and Plafker (1982) into greenschist facies phyllites outside the CMC, and schist and migmatite zone within the CMC. The last two zones and the metamorphic gradient therein form the principal focus of this paper. Analytical methods are available in Appendix A.1, mineral abbreviations used in the text, tables and figures follow Whitney and Evans (2010).

4.1. Transect 1

In Transect 1, the CMC is surrounded by phyllites (Figs. 1, 2) which are greenschist facies rocks. They have a monotonous mineralogy of chl–ep–ms–pl–q +/− bt (samples B43–44–45, T28–29, Fig. 2a).

4.1.1. Schist zone

The northern part of the CMC in transect 1 is made up of a schist zone commonly intruded by various syn- to post-tectonic plutonic bodies of different generations. In this transect the peak paragenesis of the schists is interpreted to be the fine-grained assemblage bt–pl–qz–grt–sil (samples B9-2, B39, B10, and B7 (+ms) Table 2, Fig. 3a–b). This paragenesis is overprinted by late muscovite and minor chlorite, both mainly replacing the biotite–silliminate peak fabric (Fig. 3b).

Biotite is up to 1 mm in length and defines the S2 foliation (Gasser et al., 2011; Pavlis and Sisson, 1995). Quartz and plagioclase form the fine-grained matrix in between the biotite network. Plagioclase has a typical composition of andesine which varies between $Ab_{64}An_{36}$ and $Ab_{70}An_{30}$ (Fig. A.1; Table 3a). Sillimanite, garnet and late muscovite and chlorite are the four most important minor phases. Sillimanite occurs as fibrolite and is usually spatially associated with biotite. Garnet is usually <500 μm in size and appears as euhedral to sub-euhedral grains and occurs together with biotite, plagioclase and quartz. Garnet is unzoned with a homogeneous core (~200–500 μm) and a fairly constant core composition ($alm_{71}sps_{10}prp_{13}grs_5$) with a thin rim (10–50 μm) enriched in MnO (Fig. 4a). MgO decreases from the cores to the rims whereas FeO is mostly constant, inferring an increase of

Table 1
XRF determined whole rock compositions of metapelites for the Chugach Metamorphic Complex of transects 1, 2 and 3. Typical average metapelitic whole rock compositions are below 2.5% CaO following Shaw (1956) (Gasser et al., 2012a, 2012b). T1, T3 and T2 refer to the different transects (Fig. 1b). XRF analyses are in weight % oxide.

		wt%	SiO_2	TiO_2	Al_2O_3	Fe_2O_3	MnO	MgO	CaO	Na_2O	K_2O	P_2O_5	LOI	Sum
T1	Schist	B9[a]	60.74	0.85	17.59	7.95	0.10	3.12	1.91	2.21	3.13	0.23	2.35	100.18
		B39	60.26	0.75	17.43	7.26	0.23	2.90	3.16	2.81	3.06	0.23	1.23	99.32
	Migmatite	B13	56.39	1.05	18.50	9.09	0.09	3.74	2.29	2.57	3.14	0.19	2.28	99.33
		B22[a]	60.36	0.84	17.89	7.27	0.11	2.86	2.79	3.27	2.93	0.25	0.74	99.31
		B26	62.78	0.84	16.62	7.59	0.09	3.12	2.44	2.53	2.85	0.23	0.89	99.98
		KB1[a]	61.71	0.87	16.89	6.94	0.11	2.87	3.15	3.08	2.61	0.22	1.52	99.97
		KB2	62.83	0.73	16.55	6.44	0.09	2.72	3.19	3.24	2.41	0.23	1.10	99.53
		T15[a]	68.64	0.48	15.11	4.31	0.06	1.98	3.07	3.45	1.93	0.17	0.74	99.94
T3		N38c	59.53	0.84	18.04	8.01	0.23	3.12	4.07	3.35	1.83	0.2	0.51	99.73
		N48	59.01	0.86	18.34	8.07	0.17	3.33	2.78	3.23	2.47	0.24	1.16	99.66
T2	Schist	Tk10	64.36	0.84	16.32	7.34	0.10	2.60	1.16	1.47	2.88	0.24	2.18	99.49
		Tk3	59.95	0.97	18.57	7.82	0.10	2.90	1.22	2.25	3.17	0.2	2.49	99.64
	Migmatite	Loc4	66.32	0.68	15.28	5.82	0.10	2.28	2.09	2.69	2.38	0.2	1.81	99.65
		BG4	65.05	0.76	15.43	6.36	0.09	2.41	2.18	2.32	2.37	0.05	2.07	99.09
		BG1	65.05	0.67	15.04	6.14	0.11	2.60	2.39	2.71	2.61	0.06	1.55	98.93

[a] Bulk used for Pseudosection modelling.

the Fe/(Fe + Mg) ratio from core to rim (Table 3b, Fig. 4a). The MnO-enriched rims are always concentric and their appearance is independent of the minerals surrounding the garnets (e.g. biotite, plagioclase, quartz). The concentric enrichment of MnO (feature similar to Fig. A.2) and Fe/(Fe + Mg) suggests that garnet has been resorbed (e.g. Kohn and Spear, 2000; Tracy et al., 1976). These observations corroborate that a retrograde net-transfer reaction has affected the rims of these garnets.

Muscovite occurs generally in two microstructural positions, both indicating late crystallisation and, both with a similar composition (Si ~5.95; Altot ~5.95). It occurs as (i) idiomorphic flakes that are up to 0.5 mm in size and crosscut the foliation, and (ii) fine-grained overgrowths resorbing sillimanite, quartz and biotite (Fig. 3b). Late chlorite is usually associated with biotite; ilmenite, apatite and tourmaline occur as accessory phases.

4.1.2. Migmatite zone

In transect 1, three different zones with slight Ca-rich metapelite bulk compositions have been observed in the migmatite zone (Fig. 2 and Table 2). (i) A northern migmatite zone, which has the same paragenesis as the schist zone, but with foliation-parallel leucosomes (Fig. 3c) that suggest melt was part of the peak paragenesis of grt–pl–qz–bt–sil–liq (samples B22–B23–B26, Fig. 3d). (ii) A central migmatite zone in which more leucosome is present but sillimanite is absent (peak paragenesis: grt–pl–qz–bt–liq; samples KB1–KB2–KB3, Fig. 3e). (iii) A southern migmatite zone which has the distinguishing feature of coarse muscovite in the peak assemblage (peak paragenesis: grt–pl–qz–bt–ms–liq; samples T25–T27–T15; Fig. 3f).

Table 2
Peak parageneses for each sample studied in this study used for Av*P*–*T*, RSCM and pseudosection calculations ((x): peak phase; (−) retrograde phase).

	bi	pl	qtz	grt	and	sil	ms	chl	cd
Transect 1									
Schist									
B9.2	x	x	x	x		x	−	−	
Migmatite									
B13	x	x	x	x		x			x
B23, B26, B22	x	x	x	x		x	−	−	
KB1, KB2	x	x	x	x			−	−	
T27, T15	x	x	x	x			x −	−	
Transect 2									
Schist									
Tk12	x	x	x	x	x		x −	−	
Tk10	x	x	x		x		x −	x −	
Tk3	x	x	x	x		x	x −	−	
Migmatite									
BG24, BG12, BG4, BG1	x	x	x	x			x −	−	
Loc4b, BG6, BG9	x	x	x	x		x	x −	−	
Transect 3									
Migmatite									
N35, N38	x	x	x	x			x	−	

4.1.2.1. Northern-Central migmatite zone. In the entire migmatite zone, biotite, plagioclase and quartz are similar to the schist zone and define the main foliation (Fig. 3d–f). Plagioclase compositions are between $Ab_{68}An_{32}$ and $Ab_{72}An_{28}$ (Fig. A1 and Table 3a). Garnet, muscovite and chlorite are the minor phases. Sillimanite fibrolite is only present in the northern migmatite zone and is always associated with biotite flakes and garnet (Fig. 3d). Garnet (200–500 μm in size) is slightly zoned with a homogeneous core composition and thin rims enriched in spessartine and pyrope (Table 3b and Fig. 4b). Garnet shows similar resorption features as those in the schist zone (Fig. A.2). Few and small (~0.1 mm) late muscovite crystals (Si ~6.2; Altot ~5.5) crosscut the foliation or crystallised after biotite. Minor chlorite is present in the samples and recrystallised mostly after biotite. Cordierite was found in one sample (B13), which represents a cordierite-rich pocket of different bulk composition (Table 1) and which has a peak paragenesis of sil–bt–qz–pl–grt–crd. In the central migmatite zone, rare K-feldspar has been found and appears as small-sized xenoblastic crystals (50–200 μm), which could record the local break-down of muscovite; K-feldspar is not found in equilibrium with garnet (Fig. 3e). Accessory phases are as in the previous zones.

4.1.2.2. Southern migmatite zone. From the central toward the southern migmatite zone, the paragenesis evolves from grt–pl–qz–bt–liq to grt–pl–qz–bt–ms–liq. The main (bt–pl–qtz) and minor phases (chl-Kfsp) have exactly the same chemistry and textural characteristics as in the Central migmatite zone. Muscovite in this zone has three texturally different positions: (1) associated with biotite and parallel to the main foliation that belong to the peak (Fig. 3f); (2) crosscutting the foliation, and (3) as small crystals developed after plagioclase commonly associated with zoisite crystals (similar to Fig. 3e). These 3 habits of muscovites show no important chemical variation (Si ~6.1–6.2 and Altot ~5.5–5.6). The garnets are generally comparable in size and zoning patterns (resorption at their rims) to the garnets described from the other zones, but their composition in each studied sample is slightly different with pyrope and spessartine contents showing stronger variations than in the other zones (Fig. 4c, Table 3b).

4.2. Transect 2

Compared to transect 1, the rocks of transect 2 have a more typical metapelitic composition with lower CaO-contents (e.g. White et al., 2001, Pattison and Harte 1988; Table 1) and thus have a slightly

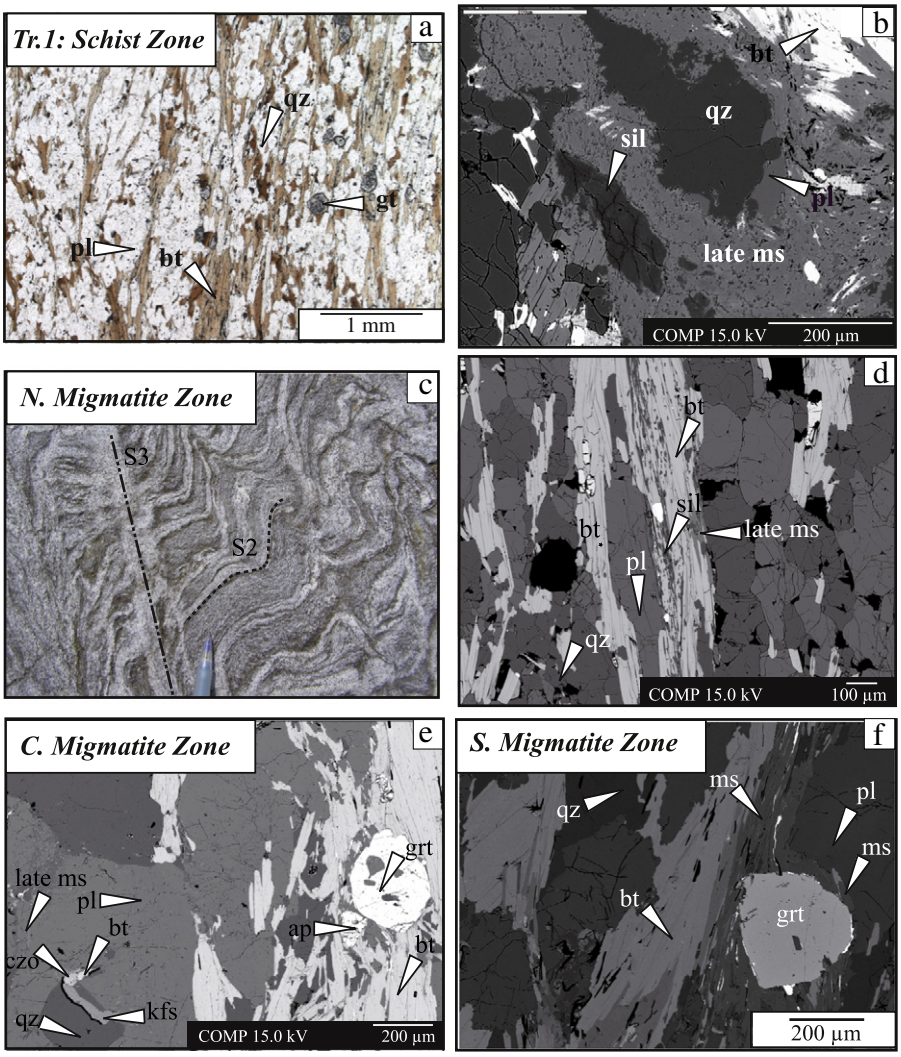

Fig. 3. Compilation of photomicrographs, outcrop photos and back scattered electron (BSE) microprobe images of rocks from the Chugach Metamorphic Complex within the schist and migmatite zones of transect 1 (a–f). (a) Representative photomicrograph for the schist zone with the paragenesis bt–pl–qz–grt (+sil) with biotite defining the foliation (B9-2 sample). (b) Sillimanite is locally replaced by a late generation of muscovite (B9-2 sample). (c) Outcrop photograph representative for the northern migmatite zone with the two ductile fabrics developed in the CMC showing the presence of melt during these two phases (pencil below-centre of image for scale, ca. 3 cm), (d) Mineral assemblage for the northern migmatite zone composed of bt–pl–qz–sil (+liq; sample B26). (e) Pictures of the central migmatite zone thin sections, which is characterised by the disappearance of sillimanite. Rare occurrence of K-feldspar xenoblast (sample KB1). (f) Mineral assemblage for the southern migmatite: bt–pl–qz–grt–ms (+liq; sample T15).

different mineralogical composition. Similar to transect 1, greenschist facies phyllites are present in the northern part of this transect and have the same characteristics as in transect 1 (samples Tk14–15; Figs. 1, 2; Table 6).

4.2.1. Schist zone

The schist zone in this transect is intruded by several large plutonic bodies (Figs. 2b, 6a). The mineralogy of transect 2 schists depends on their proximity to these plutonic bodies. When they are not in proximity to the intrusions, the schists are andalusite-rich and are uniformly composed of the inferred peak assemblage bt–pl–qz–and–ms–chl (samples Tk9, Tk10, and Tk12; Table 2). Schists in proximity to the intrusions (samples Tk2, Tk3; Table 2) have sillimanite and local garnet as part of the peak assemblage which is interpreted to be the result of contact metamorphism.

In the andalusite-bearing rocks (Fig. 5b), andalusite crystals usually contain abundant muscovite, chlorite and ilmenite, and rare biotite and plagioclase inclusions in their centre. Biotite is abundant, occurring parallel to the foliation without much variation in composition. Plagioclase varies between $Ab_{75}An_{25}$ and $Ab_{78}An_{22}$. Muscovite and chlorite are minor phases. Muscovite is present as small crystals (~20–50 µm, Si ~6.2 and Altot ~5.6) parallel to the foliation and is associated with biotite, quartz, chlorite and plagioclase (Fig. 5b). Chlorite is found in two microstructural settings: (i) as crystals similar in size to muscovite and associated with the main phases and therefore belonging to the peak assemblage and (ii) as large late flakes (up to 1 mm in size) developing in andalusite cracks. Apatite and ilmenite are accessory phases.

Schists close by intrusions are briefly described to evaluate the impact of the intrusion on their mineralogy and *T* conditions. In these schists, andalusite is replaced by a statically crystallised fabric of large muscovite flakes, sillimanite fibres and plagioclase (e.g. sample Tk3, Fig. 5c). The matrix also contains abundant large (from 300 to 500 µm) garnet (samples Tk2, Tk3) which is inferred to have developed after biotite, plagioclase and quartz (Fig. 5d). It is characterised by a homogeneous composition ($alm_{70}sps_{14}prp_{14}grs_1$; Table 3b) and is inclusion-free (Fig. 5d). Muscovite, chlorite, quartz and plagioclase in the sillimanite-bearing rocks have the same characteristics as in the andalusite-bearing samples.

4.2.2. Migmatite zone

The northern boundary of this zone is defined by the appearance of leucosome layers to the south (Fig. 5e) often associated with large

Table 3
Representative analyses of biotite, feldspar, muscovite, chlorite and garnet (wt% oxide) from the three studied transects. S, NM, CM, SM and M refer to the schist zone, the northern-, central-, southern-migmatite zones and migmatite zone, respectively. * are garnet compositions used for pseudosections in Fig. 7.

	Biotite							Feldspar								Muscovite						
	T1				T2		T3	T1						T2	T3	T1				T2		T3
	S	*NM*	*CM*	*SM*	*S*	*M*	*M*	*S*	*NM*	*CM*		*SM*	*S*	*M*	*M*	*S*	*NM*	*CM*	*SM*	*S*	*M*	*M*
	B9-2	B22	KB2	T27	Goat	BG6	N38a	B9-2	B22	KB2	KB2	T27	Goat	BG6	N35	B9-2	B22	KB2	T27	Goat	BG6	N35
SiO_2	35.63	35.18	36.13	35.47	35.11	35.55	37.39	60.5	60.48	65.19	60.31	60.06	60.97	59.96	59.03	44.23	45.72	45.25	45.42	46.41	45.37	46.01
TiO_2	2.26	2.67	1.93	2.46	1.50	1.89	1.54	0.00	0.00	0.01	0.02	0.01	0.00	0.00	0.01	0.03	1.05	1.2	0.85	0.35	0.04	0.66
Al_2O_3	19.05	19.98	18.81	18.58	20.67	19.65	18.67	24.41	24.98	18.52	25.60	25.44	25.35	25.15	25.66	37.56	34.96	34.96	34.54	35.97	35.54	34.83
Cr_2O_3	0.00	0.00	0.00	0.00	0.00	0.00	0.00	0.00	0.00	0.00	0.00	0.00	0.00	0.00	0.00	0.00	0.00	0.00	0.00	0.00	0.00	0.00
Fe_2O_3	0.00	0.00	0.00	0.00	0.00	0.00	0.00	0.10	0.16	0.15	0.03	0.00	0.18	0.08	0.01	0.00	0.00	0.00	0.00	0.00	0.00	0.00
FeO	17.81	18.77	17.41	19.07	20.01	17.42	15.59	0.00	0.00	0.00	0.00	0.00	0.00	0.00	0.00	0.43	1.06	1.00	1.38	0.94	0.80	0.98
MnO	0.11	0.18	0.17	0.28	0.14	0.05	0.01	0.00	0.00	0.00	0.00	0.00	0.00	0.00	0.02	0.04	0.00	0.00	0.03	0.01	0.00	0.00
MgO	8.83	8.7	10.02	9.68	9.2	10.29	11.99	0.00	0.00	0.01	0.01	0.00	0.00	0.00	0.00	0.21	0.57	0.43	0.85	0.39	0.57	0.89
CaO	0.00	0.02	0.00	0.00	0.00	0.00	0.00	6.59	6.12	0.00	7.27	7.07	5.68	7.27	7.56	0.62	0.00	0.00	0.00	0.00	0.01	0.00
Na_2O	0.29	0.22	0.19	0.14	0.22	0.53	0.24	7.81	8.27	0.26	7.58	7.81	8.21	8.37	7.38	0.52	0.78	1.10	0.77	1.18	1.54	1.09
K_2O	9.68	9.10	9.50	9.75	10.07	9.92	9.13	0.09	0.12	15.48	0.11	0.24	0.07	0.03	0.06	10.09	9.97	9.89	10.34	9.27	10.30	9.36
Totals	93.70	94.88	94.16	95.45	96.97	95.34	94.56	99.52	100.16	99.68	100.93	100.66	100.48	100.90	99.73	93.72	94.1	93.84	94.22	94.57	94.22	93.83
Ox.	11							8								22						
Si	2.74	2.68	2.75	2.70	2.64	2.69	2.8	2.70	2.69	3.01	2.66	2.66	2.69	2.66	2.64	5.96	6.14.	6.11	6.13	6.17	6.11	6.18
Ti	0.13	0.15	0.11	0.14	0.08	0.11	0.09	0.00	0.00	0.00	0.00	0.00	0.00	0.00	0.00	0.00	0.11	0.12	0.09	0.03	0.00	0.07
Al	1.73	1.79	1.69	1.67	1.83	1.75	1.65	1.29	1.31	1.01	1.33	1.33	1.32	1.31	1.35	5.97	5.54	5.56	5.49	5.64	5.64	5.52
Cr	0.00	0.00	0.00	0.00	0.00	0.00	0.00	0.00	0.00	0.00	0.00	0.00	0.00	0.00	0.00	0.00	0.00	0.00	0.00	0.00	0.00	0.00
Fe3	0.00	0.00	0.00	0.00	0.00	0.00	0.00	0.00	0.01	0.01	0.00	0.00	0.01	0.00	0.00	0.00	0.00	0.00	0.00	0.00	0.00	0.00
Fe2	1.14	1.19	1.11	1.21	1.26	1.10	0.97	0.00	0.00	0.00	0.00	0.00	0.00	0.00	0.00	0.05	0.12	0.11	0.16	0.10	0.09	0.11
Mn	0.01	0.01	0.01	0.02	0.01	0.00	0.00	0.00	0.00	0.00	0.00	0.00	0.00	0.00	0.00	0.00	0.00	0.00	0.00	0.00	0.00	0.00
Mg	1.01	0.99	1.14	1.10	1.03	1.16	1.34	0.00	0.00	0.00	0.00	0.00	0.00	0.00	0.00	0.04	0.11	0.09	0.17	0.08	0.11	0.18
Ca	0.00	0.00	0.00	0.00	0.00	0.00	0.00	0.32	0.29	0.00	0.34	0.34	0.27	0.35	0.36	0.09	0.00	0.00	0.00	0.00	0.00	0.00
Na	0.04	0.03	0.03	0.02	0.03	0.08	0.04	0.68	0.71	0.02	0.65	0.67	0.70	0.72	0.64	0.14	0.20	0.29	0.20	0.30	0.40	0.28
K	0.95	0.88	0.92	0.95	0.97	0.96	0.87	0.01	0.01	0.91	0.01	0.01	0.00	0.00	0.00	1.74	1.71	1.70	1.78	1.57	1.77	1.60
Sum	7.76	7.73	7.77	7.81	7.86	7.85	7.75	4.99	5.01	4.96	5.00	5.01	5.00	5.04	5.00	13.99	13.93	13.98	14.02	0.00	0.00	0.00
Or								0.005	0.007	0.968	0.006	0.014	0.004	0.002	0.003							
Ab								0.678	0.703	0.025	0.649	0.657	0.716	0.674	0.636							
An								0.316	0.288	0.000	0.344	0.329	0.274	0.324	0.360							

	Chlorite			Garnet core							Garnet rim						
	T1	T2	T3	T1				T2		T3	T1				T2		T3
	CM	*S*	*M*	*S*	*NM*	*CM*	*SM*	*S*	*M*	*M*	*S*	*NM*	*CM*	*SM*	*S*	*M*	*M*
	KB1	Goat	N38	B9-2*	B22*	KB1*	T15*	Tk2	BG9b	N35	B9-2	B22	KB1	T15	Tk2	BG9b	N35
SiO_2	30.79	23.46	26.11	38.28	38.08	38.20	38.46	35.88	37.96	37.78	38.09	38.09	38.01	38.32	36.23	37.58	37.07
TiO_2	1.57	0.03	0.06	0.01	0.01	0.02	0.04	0.02	0.00	0.06	0.00	0.00	0.02	0.04	0.14	0.00	0.01
Al_2O_3	19.76	25.15	22.19	21.33	21.49	21.67	21.65	21.17	21.36	21.56	21.39	21.67	21.61	21.56	21.14	21.03	21.85
Cr_2O_3	0.00	0.00	0.00	0.00	0.00	0.00	0.00	0.00	0.00	0.00	0.00	0.00	0.00	0.00	0.00	0.00	0.00
Fe_2O_3	0.00	0.04	0.00	0.00	0.00	0.00	0.00	0.00	0.10	0.01	0.00	0.00	0.00	0.00	0.00	0.00	0.00
FeO	20.81	28.77	19.58	31.55	30.92	30.24	29.48	32.09	32.78	28.07	31.20	29.83	30.12	27.07	32.65	31.68	30.34
MnO	0.15	0.43	0.08	4.48	6.42	4.49	5.56	6.36	1.95	5.91	5.98	8.37	5.97	10.29	5.75	6.15	4.41
MgO	11.37	11.86	18.07	3.33	2.90	4.46	3.99	2.78	5.07	3.11	2.61	2.22	3.49	2.16	3.30	3.05	3.30
CaO	0.01	0.02	0.02	1.82	1.34	1.62	2.25	1.00	1.16	4.47	1.38	1.55	1.49	2.36	0.94	1.28	3.70
Na_2O	0.06	0.03	0.03	0.07	0.02	0.00	0.01	0.02	0.02	0.00	0.01	0.05	0.00	0.05	0.07	0.01	0.01
K_2O	5.34	0.13	0.02	0.00	0.00	0.00	0.01	0.01	0.00	0.02	0.04	0.02	0.03	0.02	0.02	0.02	0.02
Totals	89.83	89.96	86.15	100.90	101.21	100.70	101.44	99.33	100.43	100.98	100.71	101.80	100.76	101.87	100.24	100.79	100.72
Ox	14			12													
Si	3.15	2.46	2.71	3.03	3.02	3.00	3.01	2.93	3.00	2.99	3.02	3.01	3.01	3.02	2.93	3.01	2.95
Ti	0.12	0.00	0.01	0.00	0.00	0.00	0.00	0.00	0.00	0.00	0.00	0.00	0.00	0.01	0.02	0.03	0.04
Al	2.84	3.10	2.71	1.99	2.01	2.01	2.00	2.04	1.99	2.01	2.01	2.02	2.02	2.01	2.02	1.98	2.05
Cr	0.00	0.00	0.00	0.00	0.00	0.00	0.00	0.00	0.00	0.00	0.00	0.00	0.00	0.00	0.00	0.00	0.00
Fe3	0.00	0.00	0.00	0.00	0.00	0.00	0.00	0.02	0.01	0.00	0.00	0.00	0.00	0.00	0.00	0.01	0.00
Fe2	1.78	2.52	1.70	2.09	2.05	2.01	1.95	2.17	2.17	1.86	2.12	2.01	2.03	1.82	2.17	2.11	2.02
Mn	0.01	0.04	0.01	0.30	0.43	0.30	0.37	0.44	0.13	0.40	0.40	0.56	0.40	0.69	0.39	0.42	0.30
Mg	1.73	1.85	2.79	0.39	0.34	0.52	0.46	0.34	0.60	0.37	0.31	0.26	0.41	0.25	0.40	0.36	0.39
Ca	0.00	0.00	0.00	0.15	0.11	0.14	0.19	0.09	0.10	0.38	0.12	0.13	0.13	0.20	0.08	0.11	0.32
Na	0.00	0.00	0.00	0.00	0.00	0.00	0.00	0.00	0.00	0.00	0.00	0.00	0.00	0.00	0.00	0.00	0.00
K	0.70	0.00	0.00	0.00	0.00	0.00	0.00	0.00	0.00	0.00	0.00	0.00	0.00	0.00	0.00	0.00	0.00
Sum	9.90	10.00	9.94	7.98	7.98	7.99	7.99	8.04	8.00	8.00	7.98	7.99	7.99	7.99	8.04	8.00	8.02
alm				71.38	70.09	67.75	65.60	70.46	72.35	61.81	71.88	67.87	68.38	61.48	70.18	70.24	65.94
and				0.00	0.00	0.00	0.00	1.08	0.19	0.00	0.00	0.00	0.00	0.00	1.98	0.46	0.00
grs				5.22	3.84	4.59	6.36	1.91	3.10	12.67	3.98	4.42	4.25	6.74	0.81	3.20	10.70
prp				13.27	11.55	17.60	15.64	11.55	20.00	12.28	10.49	8.82	13.89	8.58	13.59	12.16	13.28
sps				10.14	14.52	10.06	12.40	15.01	4.37	13.24	13.65	18.89	13.49	23.20	13.44	13.94	10.08
x(g)				0.712	0.698	0.677	0.656										
z(g)				0.052	0.039	0.047	0.064										

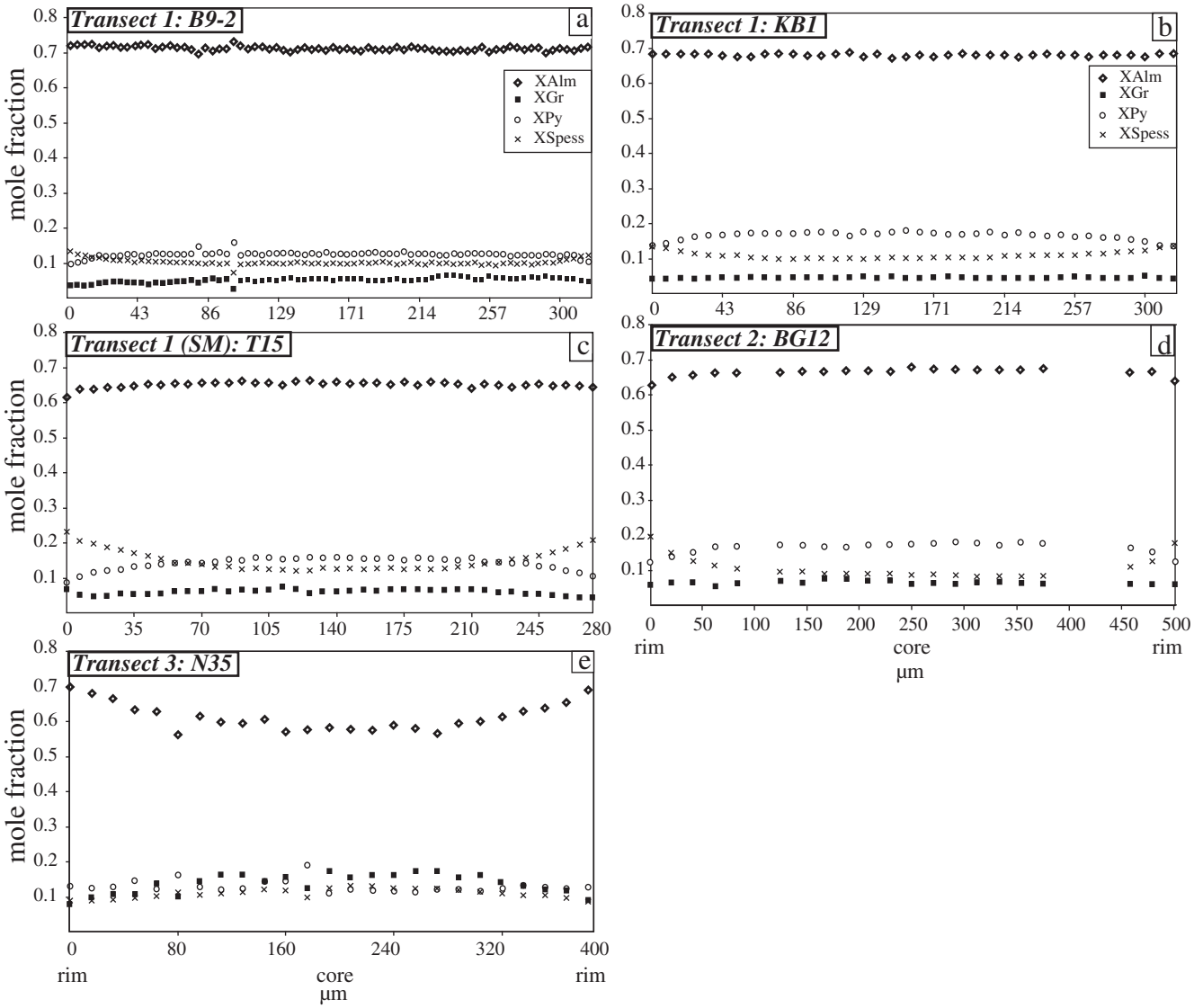

Fig. 4. Representative garnet profiles (a) from the schist zone in transect 1, (b) from the central migmatite zone in transect 1, (c) from the southern migmatite zone in transect 1, (d) from the migmatite zone in transect 2 and (e) in transect 3. Garnet end-members plotted in this figures are: almandine, pyrope, grossular and spessartine.

prismatic sillimanite crystals. Rocks of metapelitic bulk composition have a similar mineralogy throughout the transect with biotite, plagioclase, quartz, garnet, muscovite (Fig. 5f) and sillimanite being the main phases, although some samples lack sillimanite (Table 2). The inferred peak paragenesis is: grt–pl–qz–bt–ms–liq +/− sil (Table 2). Biotite is compositionally and texturally similar to the other zones (Table 3a). Plagioclase composition varies between $Ab_{72}An_{28}$ and $Ab_{68}An_{32}$ (Fig. A1 & Table 3a). Garnet is abundant, large in size (up to cm) and shows resorption features at its rim similar to those described in transect 1 (Fig. 4d and A2). Garnet composition evolves from $alm_{65}sps_{6}prp_{26}grs_{2}$ and $alm_{66}sps_{3}prp_{17}grs_{13}$ in the core to $alm_{70}sps_{14}prp_{12}grs_{3}$ at the rim. Large prismatic crystals of sillimanite (from 100 µm up to cm) are found in some samples (Loc4b, BG6, and BG9). Minor phases are muscovite, staurolite, K-feldspar and chlorite. Muscovite is quite abundant and is present in 2 different habits: (1) crystals developed parallel to the foliation and belong to the peak assemblage (0.1–0.5 mm, Fig. 5f), (2) late crystals crosscutting the foliation (0.1–0.3 mm). K-feldspar and chlorite are minor phases and occur as described in the other migmatite zones. Ilmenite, graphite and apatite are the accessory phases.

4.3. Transect 3

In contrast to the others, transect 3 does not contain a schist or phyllite zone. The south-western part of the transect is made up of amphibolites, whereas the north-eastern part is made up of migmatitic Ca-rich metapelite (Fig. 2c; Bruand et al., 2011). The peak paragenesis is comparable to the southern migmatite zone of transect 1: grt–pl–qz–bt–ms–liq (Table 2, Fig. 5g). In this transect biotite, quartz and plagioclase have similar characteristics to migmatites from transects 1–2. However, the chemistry of the garnet is different and show strong zoning between core and rim: for almandine from 60% to 70%, for pyrope from 12% to 14%, for spessartine from 13% to 9% and for grossular from 13–14% to 8% (Fig. 4d). The garnet core revealed a typical growth zoning rarely surrounded by two external rims (each about 10 µm) enriched in CaO (Fig. A.2). Muscovite, chlorite and K-feldspar are minor phases. Muscovite is commonly found (a) in minor amounts and parallel to the foliation and belongs to the peak (Fig. 5g, Si ~6.20 Al ~5.5) or (b) as big flakes (0.5–1 cm, Si ~6 Al ~5.85; Fig. 5h) crosscutting the foliation. K-feldspar occurs extremely rarely as small xenoblastic crystals (<100 µm), which developed within plagioclase

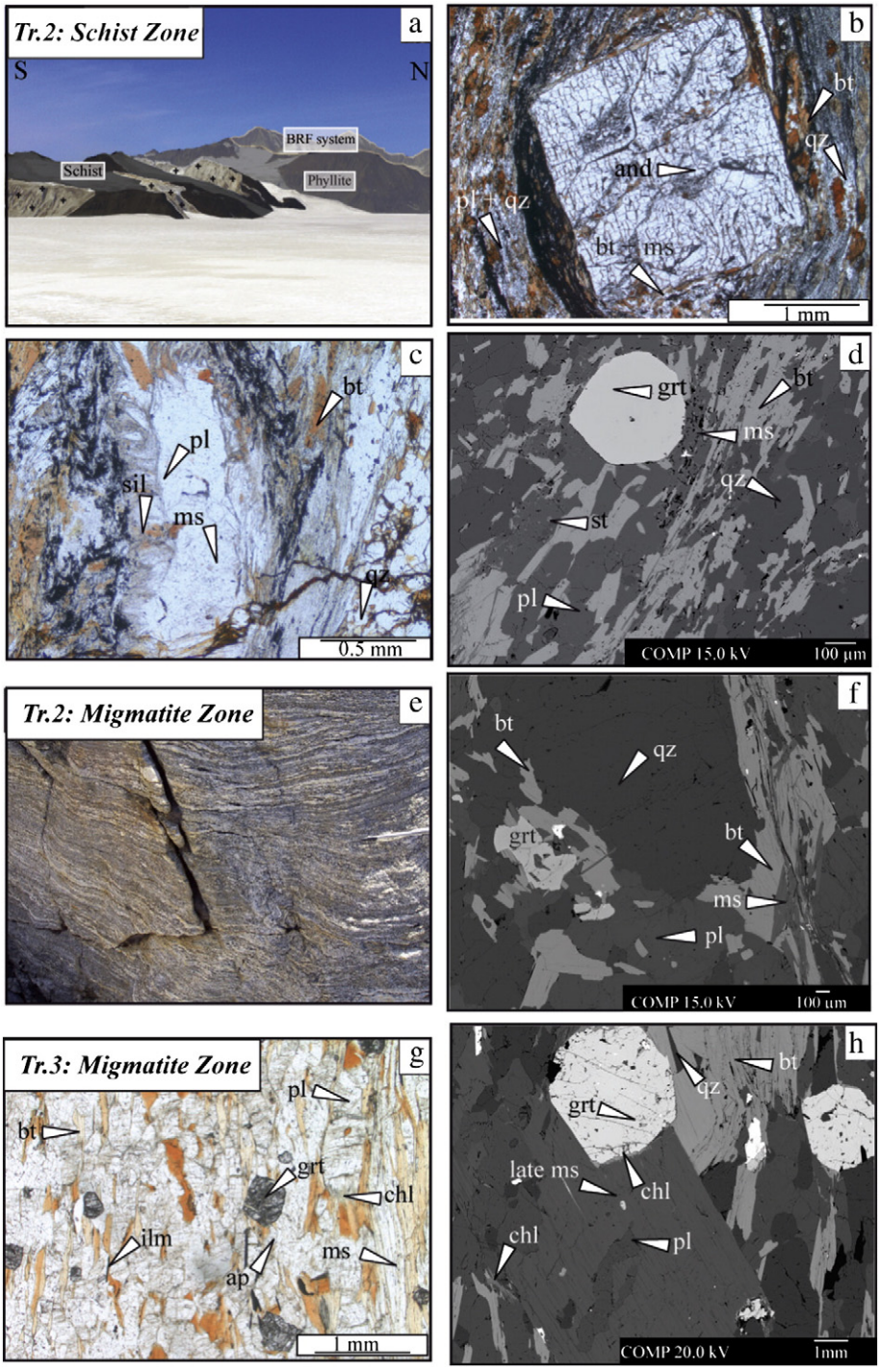

Fig. 5. Compilation of field photos, photomicrographs and back scattered electron microprobe images of rocks from the CMC within the schist and migmatite zones of transect 2 (a–f) and migmatite of transect 3 (g–h). (a) Field photo showing the plutons intruding the schist zone of transect 2. The outcrop width corresponds to about 5–6 km. (b) Representative photomicrograph for samples from the schist zone of T2 which are not affected by contact metamorphism. It shows the paragenesis and–pl–qz–bt (+ms–chl; Tk10 sample). (c–d) Representative photomicrographs for schist samples affected by the contact metamorphism with (c) an andalusite replaced by muscovite, sillimanite and plagioclase (Tk3 sample); (d) development of garnet after biotite, quartz and plagioclase (Tk3 sample). (e) Outcrop photograph representative for migmatites in transect 2. Pencil in right-centre of image for scale (ca. 8 cm). (f) Representative images for the migmatite zone with the mineralogical assemblage: bt–pl–qz–ms–grt ± sil (BG12 sample). (g) Typical mineralogical assemblage of this zone with the presence of bt–pl–qz–ms–grt (sample N35). (h) BSE image showing the development of coarse and late muscovite in sample N48 (transect 3).

and never in contact with the other minerals belonging to the peak paragenesis. Chlorite is a late phase crystallising after muscovite and biotite. Ilmenite, tourmaline, graphite, allanite and apatite are the most common accessory phases.

5. Thermobarometry

Most of our investigated samples are extremely fresh, single stage metamorphic rocks with little retrograde overprint (10–20 µm garnet

Table 4
Results from the thermobarometric calculations for the Chugach Metamorphic Complex. The left part of the table contains average *P–T* calculations using THERMOCALC, the right part of the table contains results for average *P* calculations using the temperature obtained from the grt–bt thermometry. The reaction numbers are given in Table 5. Samples are listed from north to south in each transect and sample locations are shown in Fig. 2.

	Sample	XH2O	*T* (°C)	sd	*P* (kbar)	sd	Corr	Sigfit	Reaction nb	grt–bt (°C)	*P* (kbar)	sd	Sigfit	XH2O	r. nb
Transect 1															
S	B9-2	*FI*	642	**138**	**6.1**	**2.1**	**0.82**	**0.43**	**1, 13–14**	**632**					
NM	**B13**	1	649	78	4.8	0.8	0.86	0.19	**1, 7–9, 11,12**	**638**					
		0.25	**639**	**77**	**3.8**	**0.8**	**0.86**	**0.22**							
	B23									**645**					
	B26	***FI***	**636**	**136**	**5.6**	**2**	**0.80**	**0.29**	**1,13,14**	**628**					
	B22	***FI***	**604**	**132**	**4.7**	**1.9**	**0.78**	**0.05**	**1, 13, 15**	**623**					
CM	**KB1**	**–**	**–**	**–**	**–**	**–**	**–**	**–**	**–**	**645**	**4.7**	**1.6**	**0.4**	***FI***	**13–14**
	KB2	**–**	**–**	**–**	**–**	**–**	**–**	**–**	**–**	**666**	**5.1**	**1.6**	**0.7**	***FI***	**13–14**
SM	**T27**	1	679	32	7.3	1.1	0.74	1.02	**2, 4, 5, 16–18**	**663**					
		0.75	**657**	**34**	**7.1**	**1.2**	**0.75**	**1.13**							
		0.5	635	36	7.0	1.3	0.76	1.26							
	T15	1	683	33	7.3	1.1	0.75	0.84	**2, 4, 5, 16–18**	**666**					
		0.75	**661**	**31**	**7.1**	**1.1**	**0.75**	**0.93**							
		0.5	638	31	7.0	1.1	0.76	1.03							
Transect 2															
S	**Tk12**	**1**	**543**	**23**	**3.4**	**0.9**	**0.96**	**0.35**	**2, 25–28**	**592**					
		0.75	526	22	3.4	0.9	0.96	0.28							
	Tk10	**1**	**620**	**73**	**5.1**	**2.9**	**0.98**	**1.89**	**20, 23, 24, 29–32**	**–**					
		0.75	598	73	4.9	2.9	0.98	1.98							
	Tk3	1	685	28	6.6	1.1	0.90	0.71	**1–3,10,37,38,42**	**655**					
		0.75	**662**	**27**	**6.5**	**1.1**	**0.91**	**0.79**							
		0.5	638	26	6.3	1.1	0.91	0.89							
M	**BG24**	1	803	77	10.4	2.1	0.72	1.77	**2, 4, 5, 16–18**	**695**					
		0.75	777	77	10.3	2.2	0.72	1.99							
		0.5	**751**	**80**	**10.1**	**2.3**	**0.72**	**2.08**							
	BG12	1	708	32	9.4	1.1	0.76	0.98	**5, 16–18, 33, 34**	**687**					
		0.75	**685**	**34**	**9.2**	**1.2**	**0.76**	**1.12**							
		0.50	662	36	9.1	1.3	0.77	1.28							
	Loc4b	**1**	**666**	**25**	**8.2**	**1.2**	**0.93**	**1.17**	**1, 4, 37, 38, 40, 41**	**674**					
		0.75	645	25	8.1	1.2	0.93	1.22							
	BG1	**1**	**710**	**82**	**9**	**2.8**	**0.74**	**2.79**	**2, 4, 5, 16–18**	**785**					
	BG6	**1**	**642**	**43**	**8.7**	**2.2**	**0.93**	**2.19**	**1, 4, 35, 37–39**	**654**					
		0.75	623	43	8.6	2.2	0.93	2.29							
	BG4	**1**	**717**	**43**	**10.9**	**2.1**	**0.58**	**1.4**	**2, 4, 5, 35, 36**	**757**					
		0.75	696	44	10.9	2.2	0.58	1.52							
	BG9b	**1**	**677**	**45**	**8.6**	**2.1**	**0.93**	**2.07**	**1–3, 5–6, 36–37**	**732**					
		0.75	656	45	8.4	2.2	0.93	2.19							
Transect 3															
M	**N35**	1	644	29	8.2	1	0.80	0.63	**2, 4, 5, 16–18**	**624**					
		0.75	**625**	**27**	**8.0**	**1**	**0.80**	**0.67**							
		0.50	605	26	7.8	1	0.81	0.74							
		0.25	563	24	7.5	0.9	0.81	0.96							
	N38	**–**	**–**	**–**	**–**	**–**	**–**	**–**	**–**	**625**	**8.3**	**1.2**	**0.4**	***FI***	**13nnn15**

FI = fluid-independant equilibria obtained for Av*P–T* and Av*P* calculations. Error on the grt–bt thermometer is estimated to 50 °C.

resorption zones and few late chlorite–muscovite crystals), so that there is typically little doubt as to the metamorphic peak paragenesis. Therefore, a series of thermobarometric tools using mineral compositions of the inferred peak paragenesis have been applied (Table 2). Moreover, in order to apply a method that is independent of paragenetic variations, the temperature dependence of carbonaceous material crystallisation has been used to constrain peak temperatures. The results of these applied methods are described below.

5.1. Garnet–biotite thermometry

The garnet–biotite (grt–bt) thermometer of Kaneko and Miyano (2004, 2006) which was listed by Wu and Cheng (2006) as one of the most reliable grt–bt thermometers of the last 30 years has been used. The thermometer is reported to be accurate to about ±50 °C. This thermometer uses the Fe^{2+}–Mg cation exchange experiments and non-ideal mixing properties of garnet, and is calibrated for a range of 500–750 °C. It is, therefore, applicable for the CMC (Fig. 1). The ferric iron content of biotite was estimated using the protocol of Kaneko and Miyano (2004): $Fe^{3+} = 0.11\ Fe^{T}$ for biotite coexisting with ilmenite (no magnetite). In order to apply this thermometer, the zoning of the garnets need to be understood. Garnets with unzoned homogeneous cores surrounded by a thin rim enriched in Mn and Fe/(Fe + Mg) have been commonly described in high-grade metamorphic terranes (e.g. Kohn and Spear, 2000; Tracy et al., 1976; Yardley, 1977) and are typical for garnets from transects 1 and 2 of the CMC. At high temperature (>650 °C), MnO, FeO and MgO compositions are generally homogenised through the garnet crystals by diffusion at the temperature peak and thus a potential growth zoning present in the garnet is often erased (e.g. Caddick et al., 2010; Tracy, 1982). Garnet rims of transects 1 and 2 show a typical retrograde zoning implying retrograde net-transfer reaction (Fig. 4a–d; Kohn and Spear, 2000). In these samples, the biotite modal proportion in the rock is at least two times more important than the garnet modal proportion, and cooling of the CMC is short (~5 Ma; Gasser et al., 2011) allowing only a limited amount of retrogression. According to this and details given in the petrography section, homogeneous core composition of garnets and biotite in the matrix was used for determination of peak temperature for grt–bt thermometry. Consistency between the different thermobarometry techniques (RSCM, pseudosection, Av*P–T*) further in the text shows that the results obtained with this method are reliable. In transect 3, the garnet core revealed a typical growth zoning (Fig. 4e and Fig. A.2). For this

Table 5
List of independent reactions used in THERMOCALC average *P–T* calculations in Table 4.

N°	Reactions
1	grs + qz + 2sil = 3an
2	3eas + 6qz = phl + prp + 2ms
3	7phl + 12sil = 3eas + 5prp + 4ms
4	phl + eas + 6qz = prp + 2cel
5	2ann + ms + 6qz = alm + 3fcel
6	4ann + 3fcel + 12sil = 5alm + 7ms
7	2prp + 5qz + 4sil = 3crd
8	2sps + 5qz + 4sil = 3mncrd
9	prp + eas + 3qz = crd + phl
10	ann + qz + 2sil = alm + ms
11	alm + eas + 3qz = crd + ann
12	prp + 2alm + 3eas + 9qz = 3fcrd + 3phl
13	prp + 2grs + 3eas + 6qz = 6an + 3phl
14	2grs + 3alm + 3eas + 6qz = 6an + 2prp + 3ann
15	phl + alm = ann + prp
16	ms + prp + grs = phl + 3an
17	ms + grs + alm = ann + 3an
18	3phl + 6fcel + 2 pg + 9qz = 2ab + 9cel + 2alm + 2H2O
19	3eas + 5qz = 2phl + ms + 2and
20	2eas + 5qz = phl + cel + 2and
21	eas + ames + 5qz = cel + clc + 2and
22	5phl + 5 ms + dph = 5eas + 5fcel + clc
23	ann + 2ms + 5qz = 3fcel + 2and
24	9ames + 25fcel = 12phl + 5daph + 13ms + 28qz + 16H2O
25	grs + qz + 2and = 3an
26	7phl + 12and = 5prp + 4 ms + 3eas
27	ann + qz + 2and = alm + ms
28	prp + ms + pg = phl + ab + H2O + 3and
29	phl + ame = eas + clc
30	ame + cel = clc + ms
31	10eas + dph + 25qz = 5phl + clc + 5fcel + 10and
32	4ann + 13fcel + 10 pg + 2and = 5daph + 20ab + 17ms
33	ms + 2phl + 6qz + 3cel + prp
34	2eas + 6qz = ms + cel + prp
35	2alm + 3phl + 3eas + 18qz = 5prp + 6fcel
36	2prp + 3fcel + 2 pg = 2ab + alm + 3eas + 9qz + 2H2O
37	11phl + 12sil = 5prp + 7eas + 4cel
38	3ann + 2sil + 7qz = 2alm + 3fcel
39	prp + 3ann + 2 pg + 9qz = 3alm + 2ab + 3cel + 2H2O
40	3an + pg = ab + grs + 3sil + H2O
41	ann + eas + 6qz = 2cel + alm
42	prp + ms + pg = phl + ab + 3sil + H2O

case, the outer part of the garnet core has been taken for further calculations. In all transects, the composition of matrix biotite which is not in contact with garnet crystals has been taken for the calculations to avoid potentially significant chemical interactions between these two phases (e.g. Fe–Mg re-equilibration effects, retrograde Net-transfer reaction; Indares and Martignole, 1985; Kohn and Spear, 2000).

For the schist zone and northern migmatite zone of transect 1, the average temperature retrieved is 635 ± 50 °C with no difference in temperature between the two zones (Table 4, Fig. 6). Samples from the central and southern migmatite zones yield somewhat higher temperatures of 660 ± 50 °C (Table 4).

In transect 2, calculated temperatures for the schist zone vary, depending on whether the rocks are close to the intrusions or not. Schists not close to intrusions (e.g. sample Tk12) yield temperature of 592 ± 50 °C, whereas those close to intrusions (e.g. sample Tk3) yield temperatures of 655 ± 50 °C (Table 4). The temperature increase between the schist and the migmatite zone (Fig. 6 and Table 4) is more pronounced than in transect 1 with temperature estimates rising up to 785 ± 50 °C in the southern migmatite zone.

In transect 3, temperatures are around 625 ± 50 °C and are homogeneous within the 6 km wide migmatite zone.

5.2. Average P–T calculations

In order to obtain pressures but also test the single–thermometer estimates presented above, average pressure–temperature (Av*P–T*) calculations (Powell and Holland, 1988, 1994) were undertaken from the intersection of an independent set of end-member reactions of the equilibrium assemblage using the software THERMOCALC 3.33 (Holland and Powell, 1998, recent upgrade) and the internally consistent thermodynamic dataset 5.5 (Holland and Powell, 1998, November 2003 upgrade). Activities of the different end-members used for the calculations are obtained using the software AX of Holland and Powell (1998). Calculations for each sample were done considering the minerals that belong to the peak paragenesis (Table 2 and Table A.1) and using the same biotite and garnet couples used for the thermometry discussed above plus other phases. All the calculations done on the different samples and different mineral compositions used are available in Tables A.1 and A.2. All results with good diagnostic (see Powell and Holland, 1994) are shown in Table 4.

Since it is necessary to know the activity of water for reactions involving hydrous equilibria, average *P–T* results have been calculated as a function of $X(H_2O)$ using the THERMOCALC software. In several of the samples, this was not possible as only fluid-independent equilibria could be calculated (see in Table 4 and Table A.2: B9-2, B26, B22, KB1, KB2, and N38). If calculations were not possible (e.g. not enough minerals in the assemblage such as for KB1, KB2, and N38) then the grt–bt thermometry was used to fix T to get an estimation of pressure.

In transect 1, results obtained in the schist and northern migmatite zones (Table 4) have relatively high uncertainties due to the calculations of fluid-independent reactions only. Therefore, a potential increase in temperature at the schist–migmatite transition is not resolvable. B13 (from the northern migmatite zone) is an exceptional sample containing cordierite in its paragenesis and for which $X(H_2O)$ could be as low as 0.25. For this sample, all the *P–T* results calculated for different $X(H_2O)$ values between 0.25 and 1 are within the error of the grt–bt thermometry value (Table 4, 639–649 ± 78 °C and 3.8–4.8 ± 0.8 kbar). In the southern migmatite zone, the temperature results for both samples are in the range 635–685 °C (~±30 °C; Table 4) and the pressure is ~7 kbar for $X(H_2O)$ varying between 0.5 and 1. Across the different zones of transect 1 the temperatures retrieved lie between 600 °C and 680 °C and overlap within uncertainty; they are consistent with the bi–grt results discussed above (Fig. 6). Pressures across the transect vary from ~6.1 kbar in the schist zone, between 3.8 and 5.6 kbar in the northern and central migmatite zones and ~7.1 kbar in the southern migmatite zone. Considering uncertainties, pressures overlap around 6 kbar except for the B13 sample (Table 4 and Fig. 6).

In transect 2, *P–T* estimates in the schist zone are ~550–650 °C and 3–6 kbar. In the schist zone, calculations on sample Tk10, which is an andalusite-bearing sample, reveal the same order of temperature and pressure range as for Tk3 (for similar $X(H_2O)$), which is a sillimanite-bearing rock. However, considering the uncertainties on these *P–T* estimates, one or the other of these aluminosilicates could be stable (Table 4). In the migmatite zone, *P–T* values are 650–750 °C and 8–11 kbar. For all zones, within uncertainties the temperatures obtained using average *P–T* are mostly in the same range as bi–grt results, and are best consistent for $X(H_2O)$ around 0.75–1. An exception is BG24 where results obtained using $X(H_2O) > 0.5$ yield temperatures ~100 °C higher than those calculated with the grt–bt method. For this sample, the results converge with $X(H_2O)$ around 0.50.

In transect 3, temperature obtained from sample N35 is ~625–645 °C for $X(H_2O)$ between 0.75 and 1 and is consistent with the grt–bt thermometer results. Pressures for both samples (N35 and N38) are similar (~8 kbar). Lower $X(H_2O)$ values are unlikely as N35 is a migmatite sample and partial melting could not have occurred at conditions calculated with low $X(H_2O)$ values of 0.25–0.50 (Table 4). These results are in the same range as those for the southern migmatite zone in the other two transects.

In summary, there is no *P–T* gradient resolvable along transect 3 or across the schist–migmatite transition in transect 1 when considering uncertainties. But there is an increase in grade along transect 2 from the schist zone in the north to the southern end of the metamorphic

Table 6
Results of temperature calculations for carbonaceous material spectra for the Chugach Metamorphic Complex. R2 = D1/(D1 + G + D2) with D1, G and D2 representing different peaks of the Raman spectrum (Beyssac et al., 2002, 2003). Sp is the number of spectra, and the temperature is calculated with the geothermometer equation T (°C) = 641–445 × R^2 with a correlation coefficient R^2 = 0.96.

	Metamorphic assemblage with qz–pl		R2		Temperature (°C)	
Sample		Sp	Mean	SD	Mean	1σ
T1						
B45	bt–chl–ep–ms	17	0.21	0.05	547	5
B44	bt–chl–ep–ms	14	0.24	0.06	535	7
B43	bt–chl–ep–ms	12	0.28	0.05	515	6
B39	bt–grt–sil	11	0.10	0.04	597	6
B10	bt–grt–sil	11	0.05	0.02	620	3
B7	bt–grt–sil–ms	–	–	–	>640	–
KB3	bt–grt	–	–	–	>640	–
T25	bt–amph	–	–	–	>640	–
T28	bt–chl–ep–ms	14	0.48	0.05	432	6
T29	bt–chl–ep–ms	16	0.43	0.05	448	6
T2						
Tk15	bt–chl–ep–ms	11	0.26	0.04	526	5
Tk14	bt–chl–ep–ms	15	0.24	0.03	536	4
Tk9	bt–grt–and–ms–chl	–	–	–	>640	–
Tk2	bt–grt–ms	–	–	–	>640	–
cp						
N17	bt–grt–ms	12	0.06	0.05	613	6
N18	bt–grt–ms	12	0.08	0.05	607	6
N7	bt–grt–ms–cal–ep	–	–	–	>640	–
N33	bt–grt-ms–cal–ep	–	–	–	>640	–
N44	bt–grt–ms	–	–	–	>640	–

R2 = D1/(D1 + G + D2) with D1, G and D2 which represent the different peak areas (Beyssac et al., 2002, 2003). Sp is the number of spectra and temperature is calculated with the thermometer equation: T(°C) = *641 − 445R2* with a correlation coefficient R^2 = 0.96.

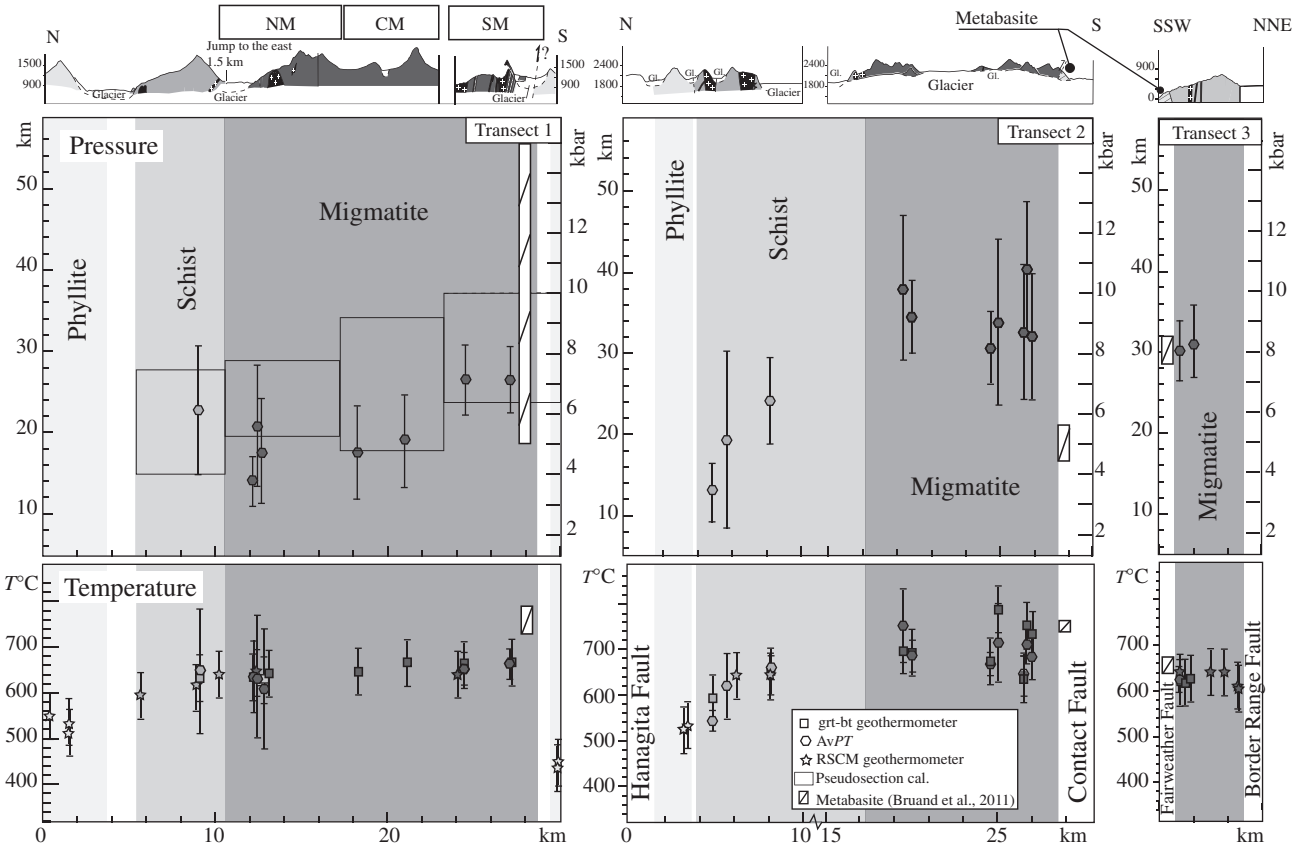

Fig. 6. North–south cross-sections through the Chugach Metamorphic Complex for all three transects studied here (see Fig. 2 for location) with results of the different thermobarometric methods. Pressure estimates of Av*P–T* calculations with corresponding error bars (±2σ; Table 4). Av*P–T* values reported for temperature are the ones in bold in Table 4. Error bars on the temperature are ±50 °C for the RSCM (Raman Spectroscopy on Carbonaceous Material) and for the grt–bt thermometer. The square fields in transect 1 correspond to pseudosection calculations (peak parageneses fields) for the different zones within this transect (Fig. 7).

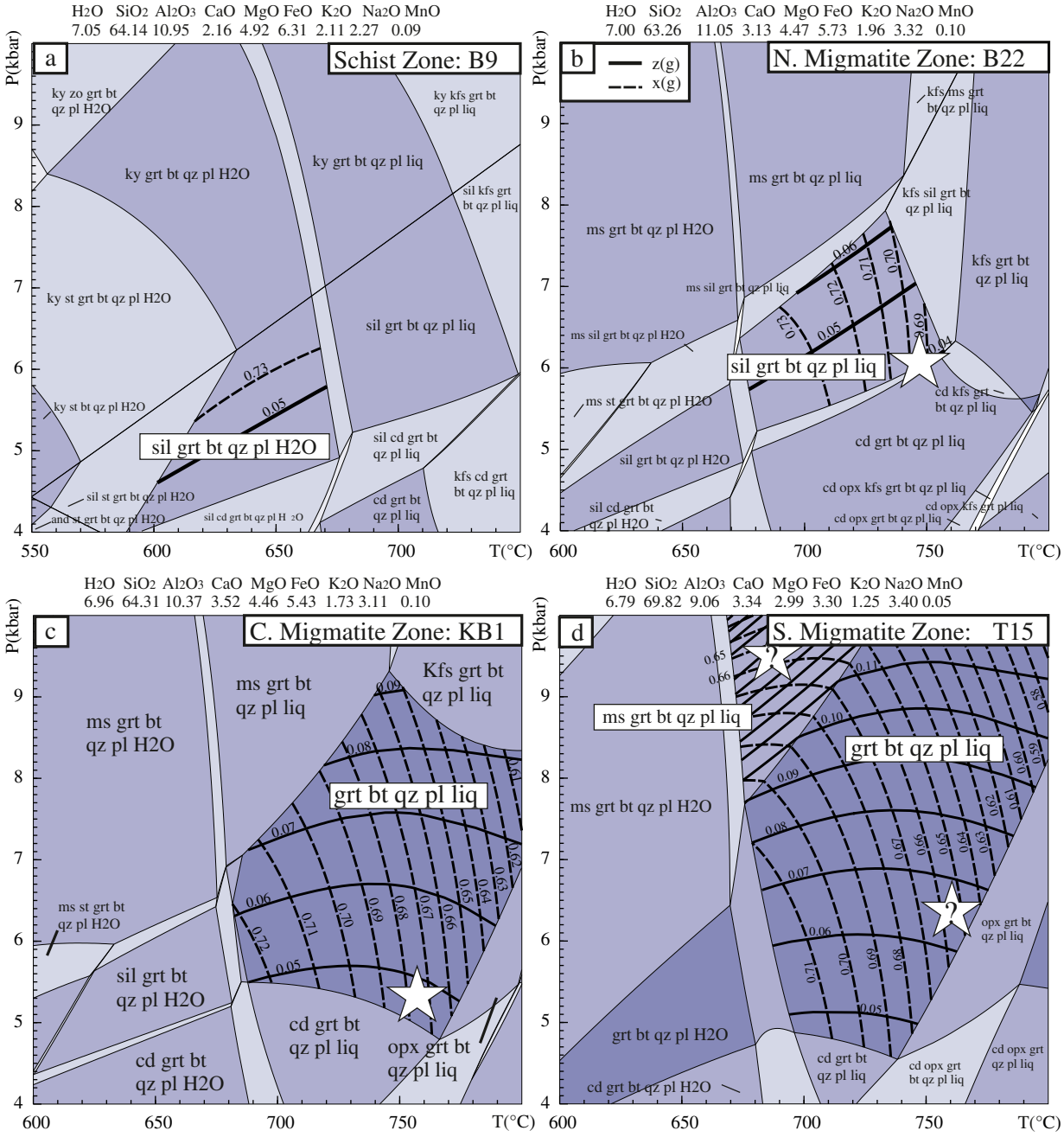

Fig. 7. Pseudosection for metapelitic compositions representative for four different samples in transect 1 (Table 1). The following solution models were used: Diener et al. (2007) for amphiboles; White et al. (2005) for biotite and garnet; White et al. (2007) for melt; Mahar et al. (1997) and Holland and Powell (1998) for cordierite, chloritoid and staurolite; Holland and Powell (1998) for spinel; Holland et al. (1998) for chlorite; Coggon and Holland (2002) for muscovite and paragonite; Powell and Holland (1999) for orthopyroxene; Holland and Powell (2003) for plagioclase and K-feldspar. (a–d) Pseudosections for the different zones recognised in transect 1. Assemblages are labelled and isopleths of garnet (x(grt) = Fe/(Ca + Mn + Fe + Mg)—dashed lines and z(grt) = Ca/(Ca + Mn + Fe + Mg)—bold lines) are drawn in the fields of interest. Stars indicate garnet compositions of the samples (* compositions in Table 3b). In (d) both stars are giving potential *P–T* conditions of the rock depending on garnet composition and whether muscovite is stable or not. See discussion in the text.

complex from ~550 °C and 3.5 kbar toward up to ~750 °C and 11 kbar (Fig. 6). Most of the samples reveal reliable results for calculations done with $X(H_2O)$ about 0.50–1 and are consistent with the bi–grt results. High $X(H_2O)$ values imply that water-rich conditions must have been present at peak metamorphic conditions in the localities studied here. Lower $X(H_2O)$ for most of the samples results in much lower temperatures, which are too low to produce partial melting in the migmatite rocks. These results would also be inconsistent with the bi–grt results obtained in this study. Importantly, calculations with different $X(H_2O)$ values do not affect the *P* estimates, which are in general higher in the southern part of the CMC. Water-rich conditions at the metamorphic peak are also suggested by (1) the apparent low temperature conditions for melting (650–700 °C) which indicate a melt that is still H_2O-rich, and (2) the low amount or absence of muscovite at the peak in the schists as well as the absence/low amount of muscovite at the peak in the migmatites and thus the minor importance of muscovite-breakdown melting (e.g. Berger et al., 2008; Sawyer, 2010; Yardley and Barber, 1991).

5.3. Raman spectroscopy on carbonaceous material (RSCM)

The RSCM method (Beyssac et al., 2002), using the temperature dependence of progressive transformation of organic matter into graphite (Wopenka and Pasteris, 1993) provides a useful comparator to results derived from conventional thermometry. It has been applied to the samples from the three transects and in addition to estimate temperatures in the phyllites surrounding the CMC. Carbonaceous material is abundant in these rocks and has been analysed for comparison with the CMC rocks. The calibration of Beyssac et al. (2002, 2003) has been used, to determine the temperature of the samples, applicable in the temperature range of 330–640 °C.

In transect 1, RSCM thermometry reveals two major temperature changes: one in the north between the phyllite zone and the schist zone, and one between the southern migmatite zone and the phyllites to the south (Fig. 6, Table 6). In the north, there is an increase of ~70 °C between the phyllites and the schist zones from ~530 °C to 600 °C (Table 6). Further south within the migmatite zones, graphite is fully crystallised suggesting that temperatures are above 640 °C (Beyssac et al., 2002). In the south, there is an important temperature decrease (by ~200 °C within a distance of 1 km) between migmatites and the phyllites (Fig. 6). The higher temperatures in the northern phyllites compared to those in the south is in agreement with the presence of biotite in the northern phyllites and its absence in the southern phyllites.

In transect 2, all samples from the migmatites were metamorphosed above 640 °C (see above). Therefore, only the samples from the phyllite and schist zones were analysed. In the northern part of transect 2, the phyllites (samples: Tk15–Tk14, Table 6) show temperature values comparable to the ones of transect 1 (~530 °C, Table 6). A temperature increase of about 50–100 °C is possible between the phyllites and the schists (Table 6). A sillimanite-bearing sample was analysed close to an intrusion (sample: Tk2) and an andalusite-bearing sample with a paragenesis which seems not to have been affected by the contact metamorphism (Tk9). Both samples show perfect graphite crystals (T >640 °C). Consequently, RSCM thermometry from this andalusite-bearing schist reveals higher peak temperatures than derived from the metamorphic peak paragenesis for andalusite-bearing samples from the same area (e.g. samples: Tk12, Table 6). This would indicate that andalusite is stable in sample Tk9 outside of its normal P–T range stability field, which has been already commonly observed in contact metamorphic areas (e.g. Cesare et al., 2003; Pattison, 1992 and references therein).

In transect 3, the northern part of the gneiss zone (N17–N18) shows temperatures around 610 °C which is ~30 °C lower compared to the rest of the transect (Table 6, Fig. 6). Throughout the remaining migmatite zone graphite is fully crystallised corresponding to temperature conditions higher than 640 °C.

6. Thermodynamic modelling

The different thermobarometric methods applied above give consistent results for the investigated transects. While a P and T increase is clear between the schist and migmatite zones of transect 2, P–T results from transect 1 from the schist and migmatite zones all overlap despite the different metamorphic zones in the field. To investigate the different metamorphic zones observed in transect 1 in more detail, and confirm the P–T range obtained with the previous methods used in this work, four metapelitic samples representative of each zone along transect 1 (Schist–NM–CM–SM) were investigated using THERMOCALC Software. Pseudosection calculations were undertaken in the following chemical system: $MnO–Na_2O–CaO–K_2O–FeO–MgO–Al_2O_3–SiO_2–H_2O$ (MnNCKFMASH).

The pseudosections were calculated in the P–T range 4–10 kbar/550–750 °C for the schist sample and 4–10 kbar/600–800 °C for the migmatite samples. Activity models used for the calculations are listed in the caption for Fig. 7. For each sample studied in this section, the whole rock XRF data has been used (Table 1). The pseudosections are calculated with just enough water in the P–T range to saturate all the sub-solidus fields.

The resulting pseudosections (Fig. 7) are well-suited to interpret the rocks described here and reflect most of the petrographic observations described above. In the schist pseudosection (Fig. 7a), the peak paragenesis (grt–pl–qz–bt–sil–H_2O) is present in a P–T range around 4–7 kbar and 580–675 °C. Kyanite is stable in the higher P portion of the pseudosection. Cordierite appears in the lower P portion as well as andalusite, which is confined to a narrow area around 4–4.5 kbar and 550–575 °C. In up temperature, garnet disappears around 570 °C and 5 kbar. In the pseudosection for the northern migmatite zone (Fig. 7b), the peak paragenesis grt–pl–qz–bt–sil–liq occurs in a P–T range around 680–760 °C and 5.2–7.9 kbar. Muscovite and cordierite are present in the higher and lower P portions of the pseudosection, respectively. In the central migmatite zone pseudosection (Fig. 7c), the peak paragenesis grt–pl–qz–bt–liq is present in a wide P–T range around 690–> 800 °C and 4.8–9.2 kbar. As in the other pseudosections, muscovite and cordierite are stable in the upper and lower parts, respectively; sillimanite appears below 700 °C. In the pseudosection for the southern migmatite zone sample (Fig. 7d), the peak paragenesis inferred from the petrology ms–grt–pl–qz–bt–liq is present above 7.5 kbar and >670 °C. Muscovite is constrained to the higher P fields of the pseudosection and cordierite to the lower P fields; sillimanite is not present.

The different peak assemblages along transect 1 record T >580 °C and P >4 kbar. From the schist zone (580–670 °C and 4–6.9 kbar) toward the migmatite zone, temperature increases across the solidus, but peak paragenesis fields for the migmatites from the different zones overlap in a wide P–T window (Fig. 7). Isopleths for garnet compositions ($x(grt) = Fe/(Ca + Mn + Fe + Mg)$ and $z(grt) = Ca/(Ca + Mn + Fe + Mg)$, Table 3b and Fig. 7), may be used to narrow the P–T peak estimates. The exact values of x(grt) and z(grt) are found in their respective peak paragenesis fields for the northern and central migmatite zone samples (stars Fig. 7b–c). For the schist zone sample (Fig. 7a), there is a slight discrepancy between the x(grt) isopleth value given by the modelling in the peak paragenesis field ($x(grt) = 0.73$) and the sample value ($x(grt) = 0.71$). In the southern migmatite zone, muscovites parallel to the foliation have been interpreted as being in equilibrium with the peak metamorphism. However, The pseudosection modelling gives garnet isopleths (x(grt) and z(grt)) comparable to the natural ones from the sample for a ms-free assemblage (Fig. 7d). In the ms-bearing field, the z(grt) value is different compared with the natural sample. The presence of muscovite in the peak paragenesis would lead to higher pressure estimates, whereas the x(grt)/z(grt) values in the ms-free field suggest higher temperature. Both the ms-bearing and the ms-free fields occur in the 6.3–9.7 kbar and 670–755 °C P–T range (Fig. 7d).

In summary, there is generally a good correspondence of the x(grt) and z(grt) values between the pseudosection and the natural samples (Fig. 7 and Table 3b). From the x(grt) and the z(grt) isopleths of the peak parageneses, the following P–T conditions have been estimated for the different zones: 4.5–6.9 kbar and 600–670 °C for the schists, 6 kbar and ~750 °C for the northern migmatite zone, ~5.5 kbar and ~755 °C for the central migmatite zone, and ~6.3–9.7 kbar and ~670–755 °C for the southern migmatite zone. Temperatures in the different migmatite zones are homogeneous and pressure estimates most likely overlap around 6 kbar. A higher pressure of up to 10 kbar for the southern migmatite zone is possible but cannot be confirmed or excluded with the current samples. The temperature estimates obtained from the pseudosection modelling are slightly higher than those retrieved by thermometry (Figs. 7 and 9).

7. Discussion

The new P–T estimates derived in this study greatly enhance our understanding of the tectonic evolution of the CMC, since they are the first

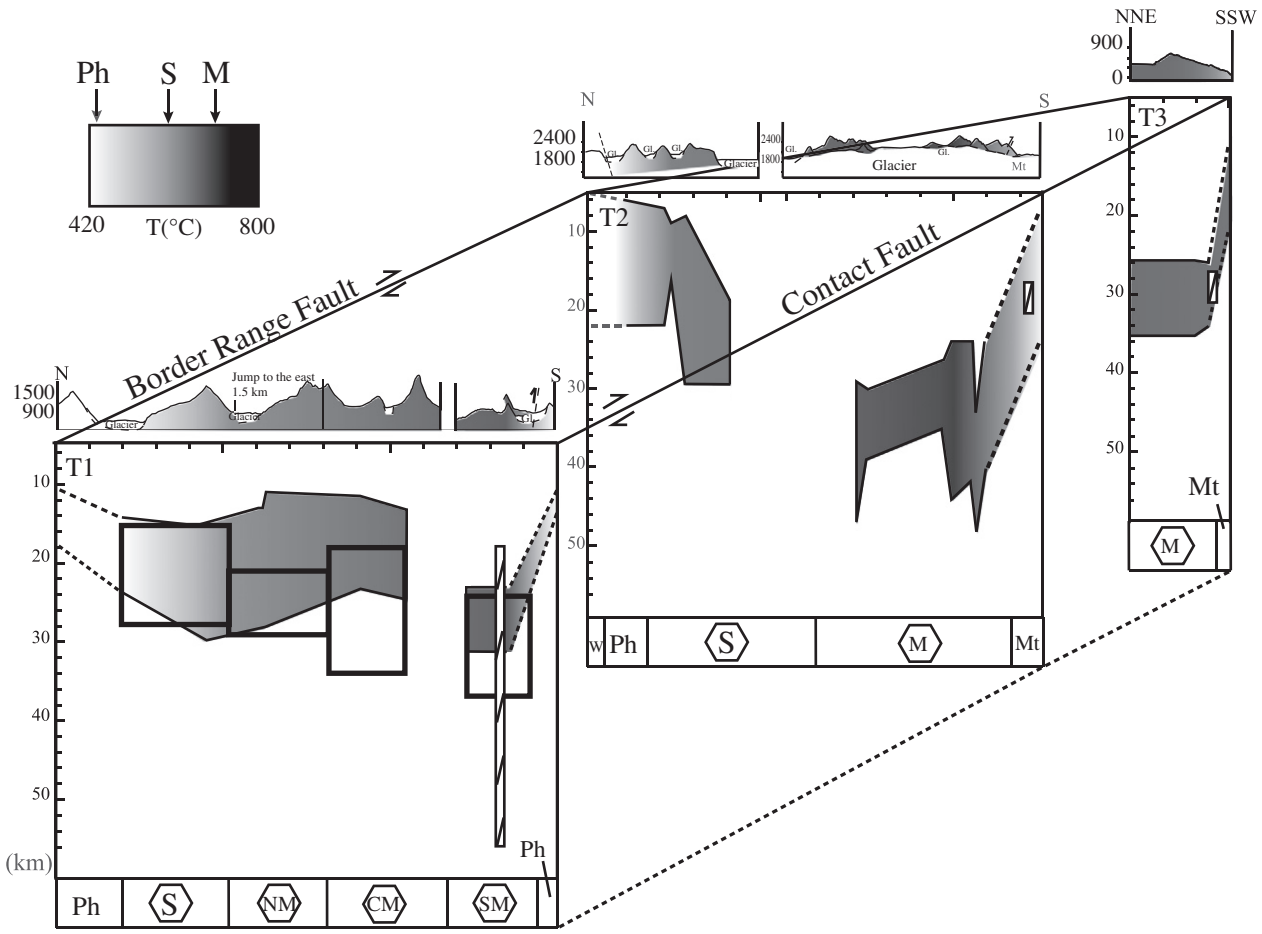

Fig. 8. Schematic sketch of the Chugach Metamorphic Complex showing the *P–T* variations along the 3 transects studied. Pressure is converted into depth using a mean rock density of 2700 kg/m^3 and assuming a lithostatic pressure. Corresponding temperatures are indicated by the white-black scale from the coldest conditions (greenschist facies phyllite at about 420 °C) to the hottest conditions (southern migmatite zone at about 800 °C) along the transects. W = Wrangellia, Ph = phyllite, S = schist, M = migmatite, Mt = metabasalt, BRF = Border Range Fault, CF = Contact Fault. *P–T* data reported are the Average *P–T* results from Table 4. *P* estimates from pseudosection modelling are also indicated by the bold squares. White bars with stripes are *PT* estimates for the metabasite belt from Bruand et al. (2011).

P–T estimates covering the complex from west to east. They are relevant for two aspects of the tectonic interpretation of the CMC. Firstly, the *ratios of metamorphic temperature to pressure* can be discussed in terms of heat source. Secondly, the derived *metamorphic pressures* and their changes along- and across-strike of the complex can be interpreted in terms of burial depth (ignoring the possibility of tectonic overpressures as the rocks are of high metamorphic grade and thus likely to be weak). In connection with the structural history of the complex this may be interpreted in terms of exhumation processes. In the following subsection, we first sum up the new *P–T* pattern derived for the CMC, and then briefly discuss the potential consequences for heat sources and exhumation mechanisms.

7.1. Summary of P–T pattern

The *P–T* estimates presented above reveal both temperature and pressure differences across- and along-strike of the CMC (Figs. 6, 8). In transect 1, pressure values overlap around 6 kbar, but there is an increase in temperature from a minimum of 600 °C in the north of the complex to a maximum of 750 °C in the south, with a clear drop in temperature to about 450 °C in the southern phyllite zone (Figs. 6, 8). In transect 2, results reveal a clear gradient in both *P* and *T* (Fig. 6). Estimated pressures increase from about 3 kbar in the north to up to 11 kbar in the south of the transect, whereas temperature increases from ~550 °C to 750 °C (Figs. 6, 8). Finally, in the narrow transect 3, pressure estimates are around 8 kbar at temperatures of ~600–650 °C (Figs. 6, 8). Using a simple first-order pressure-to-depth conversion for crustal rocks (depth = 3.7 × kbar), the estimated burial depths lie between 10 and 25 km for transect 1, 10–40 km for transect 2, and around 30 km for transect 3 (Figs. 6, 8).

South of the migmatitic gneisses, a metabasite belt which may have played a role in the exhumation of the CMC is exposed (e.g. Bruand et al., 2011; Tetreault and Buiter, 2012; Fig. 1b). In transect 1, the metabasite occurs as layers within the southern part of the migmatite zone, whereas south of transects 2 and 3 it occurs as a thick belt (several 10 of metres). *P–T* data available for the metabasite belt (Figs. 6, 8; Bruand et al., 2011) are comparable with the metamorphic conditions obtained on metapelites of the CMC for transects 1 and 3 (Fig. 6). In contrast, in transect 2, the metabasites experienced lower pressures (~5 kbar) than the metapelites (~11 kbar) to the north (Fig. 6).

7.2. Metamorphic T/P ratios: constraints on the heat source

To interpret metamorphic temperatures in terms of heat sources, temperature must be viewed in relationship to depth. In general, the ratio of metamorphic temperature to pressure is a more powerful tool for tectonic interpretation than temperatures in isolation. All the new data and data from the literature (Sisson et al., 1989) are shown on Fig. 9. Overall, Fig. 9 shows that migmatites and schists experienced metamorphism over a range of 200 °C between 550 °C and 750 °C and a pressure range corresponding to a depth range of over 30 km between 10 km and 40 km depth. Expressed in terms of *T/P* ratios,

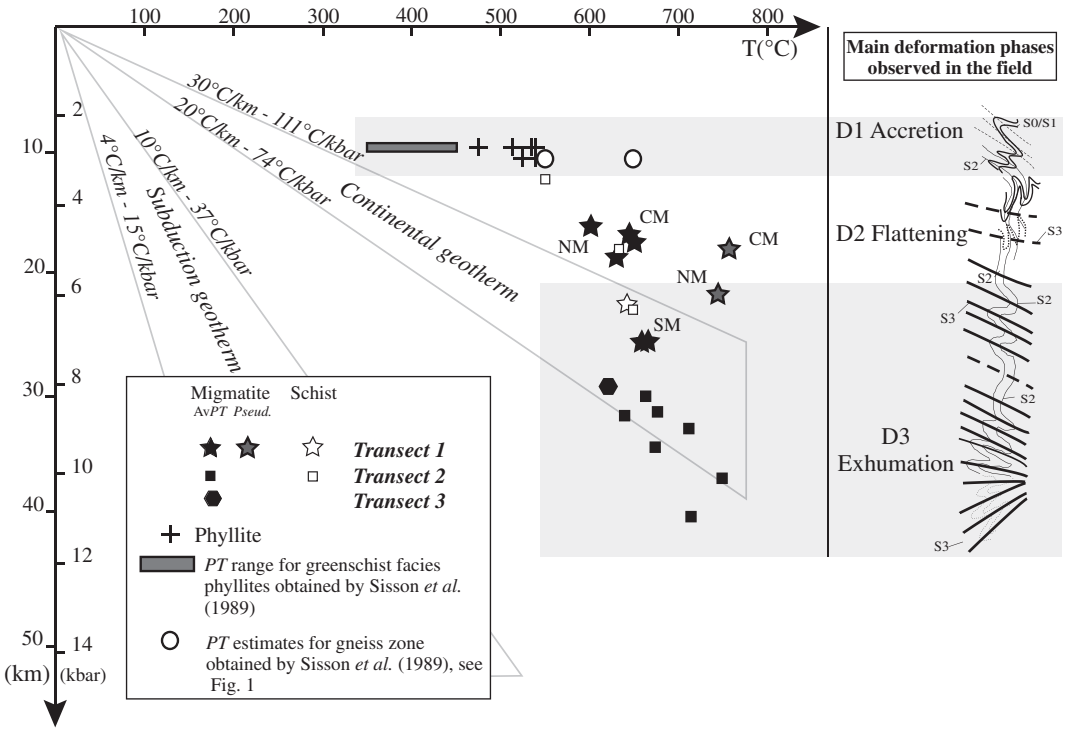

Fig. 9. Depth–temperature diagram with the compilation of average *P–T* data for transects 1, 2 and 3 (Table 4) and *P–T* data obtained with pseudosection modelling for some of the transect 1 samples, also showing some data from the literature (Sisson et al., 1989; see Fig. 1b). Pressure estimates reported for phyllite samples are 2–3 kbar (Sisson et al., 1989; Vrolijk, 1987). Right side of the figure: the sketches represent the different deformation phases that affected the CMC, and which were responsible for the different *T*/*P* ratios observed in the different zones (see text for details).

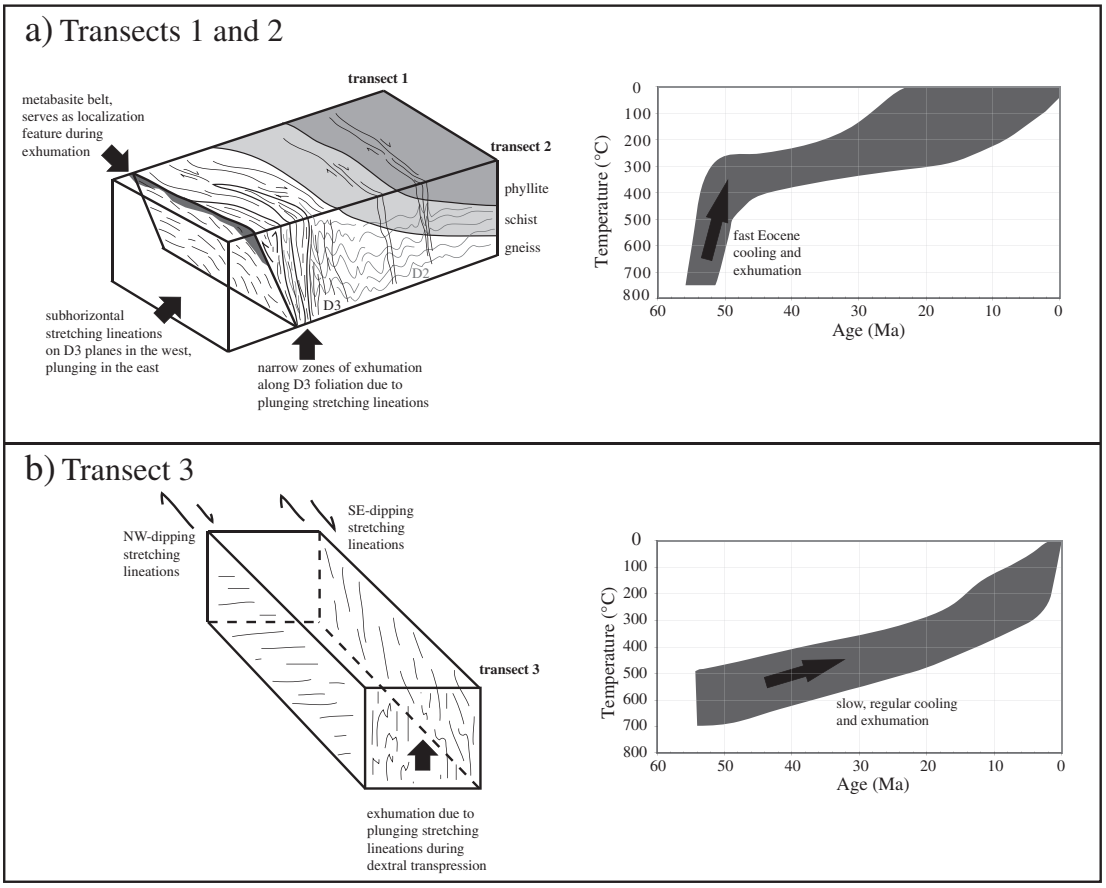

Fig. 10. 3D structural sketches of phyllite and CMC for the 3 transects studied in this contribution, modified from Gasser et al. (2011). Cooling curves are after Gasser et al. (2011, 2012).

phyllites outside the CMC and schists have ratios exceeding 111 °C/kbar while migmatites are thermally somewhat less perturbed with *T*/*P* ratios between 65 °C/kbar and 111 °C/kbar. Interpreting these *T*/*P* ratios is not straightforward, since they may have equilibrated at different times. Indeed, the structural evidence suggests that peak *P*–*T* conditions were not reached simultaneously at the different metamorphic levels: peak metamorphic conditions in the greenschist–facies phyllites outside the CMC were probably reached during D_1 associated with accretion of the sediments at ca. 60–55 Ma (Fig. 9; Gasser et al., 2011; Sisson et al., 1989), whereas peak metamorphic conditions in the schists and migmatites of the CMC were reached during the younger, short-lived D_2 and D_3 deformation events at ca. 55–51 Ma (Fig. 9; Gasser et al., 2012a, 2012b; Pavlis and Sisson, 1995). The *T*/*P* ratios are therefore discussed separately for these two different metamorphic levels.

7.2.1. Phyllite outside the CMC

Phyllites outside the CMC are characterised by a south-dipping foliation (S_1) developed during the accretion of the Chugach terrane and elevated *T*/*P* ratios (Fig. 9; >111 °C/kbar), which is unusual for generally relatively cold subduction zone settings (~15–37 °C/kbar; Maruyama et al., 1996). Sisson and Hollister (1988) and Sisson et al. (2003) interpreted these elevated *T*/*P* ratios as the result of the circulation of hot fluids through the accretionary prism, related to the subduction of young oceanic crust prior to subsequent subduction of an inferred spreading ridge during D_2 and D_3. However, the thermal state of a particular accretionary prism depends on many factors such as accretion and erosion rates, the amount of underplated sediments, the coefficients of basal friction, the fluid/lithostatic pressure ratios or the age (and therewith temperature) of the down-going plate (e.g. Barr and Dahlen, 1989; James et al., 1989). Since accretion rates in the Chugach terrane were very high and occurred over a short timescale (e.g. Sample and Reid, 2003), basal shear and/or internal strain heating could be envisaged for the origin of the elevated gradient within the phyllites outside of the CMC (e.g. Gasser et al., 2011). In any case, the high *T*/*P* ratio during the accretion of the prism may have aided the development of the later upper amphibolite facies metamorphism within the CMC.

7.2.2. T/P variations within the CMC

Within the CMC, *T*/*P* ratios from the schists in transects 1 and 2 are close to or above 111 °C/kbar (Fig. 9). Similarly, the northern and central migmatites of transect 1 have *T*/*P* ratios which are somewhat higher than the ratios from the migmatites of the other transects. These high *T*/*P* ratios might be partly inherited from the high *T*/*P* ratios already present during accretion of the sediments (ca. 60–55 Ma). In addition, the D_2 deformation event (ca. 55–51 Ma) has probably amplified the already high gradients: during this event, the schist zone and parts of the migmatite zone were vertically thinned, therewith compressing the isotherms and leading to high *T*/*P* ratios (e.g. Gasser et al., 2011; Pavlis and Sisson, 2003).

The remaining *P*–*T* data from the migmatites of transects 2 and 3 show a much larger variation in pressure for similar temperature (650–750 °C, Fig. 9) corresponding to *T*/*P* ratios between ~65 °C/kbar and 90 °C/kbar. This means that deep-level rocks appear only marginally thermally perturbed and the degree of thermal perturbation decreases with increasing depth. This is opposite to what would be expected if heating from below was the heat source for the development of the CMC migmatites. With a subducting ridge, which is generally accepted to be the cause for the CMC metamorphism (e.g. Bradley et al., 2003; Scharman et al., 2012; Sisson and Pavlis, 1993; Sisson et al., 1989), the deepest crustal levels should be substantially more perturbed than the shallower levels (e.g. Groome and Torkelson, 2009), which is not observed in Fig. 9. Moreover, after the passage of a subducting ridge, the characteristic time scale of cooling within the accretionary prism would be several tens of m.y. (e.g. Groome and Torkelson, 2009; Iwamori, 2000) even considering a rapid passage of the ridge. In contrast, Gasser et al. (2011) have shown that the CMC cooled down from 650–700 °C to ~350 °C very rapidly (between 54 and 48 Ma) shortly after the metamorphic peak in transects 1 and 2. The *T*/*P* ratios shown in Fig. 9, therefore raise significant concerns about the model of ridge subduction for the development of the CMC.

7.3. Implications for the exhumation history of the CMC

The newly derived pressure estimates for the CMC are considerably higher than the previously available *P* data which was limited to the northern and western parts of the complex (Figs. 1b, 9; Sisson et al., 1989). The pressure estimates presented in this study indicate that at least parts of the CMC were buried to considerable depths, and must have experienced subsequent exhumation. Integrating the pressure estimates with the structural history of the area allows us to discuss potential exhumation mechanisms for the CMC.

7.3.1. The role of D_3 and post D_3 shear zones

Peak metamorphic conditions in the CMC, including partial melting and maximum burial depths in the gneiss zone, were reached during a short time interval at ~55–51 Ma (Gasser et al., 2011, 2012a). These conditions were accompanied by two subsequent deformation phases: D_2 and D_3. During D_2, the accretionary prism was vertically thinned and stretched parallel to the margin, leading to the relatively high *T*/*P* ratios in the schist and parts of the gneiss zone (Fig. 9). Potential explanations for the origin of this D_2 deformation event are discussed in detail by several authors (e.g. Gasser et al., 2011; Pavlis and Sisson, 1995, 2003; Scharman et al., 2011, 2012; Sisson and Pavlis, 1993) and are not repeated here. More importantly, maximum burial depths and subsequent exhumation of parts of the gneiss zone occurred during D_3 (e.g. Gasser et al., 2011).

The D_3 deformation phase has been widely described as an overall dextral transpressional phase, with both localised subvertical shear zones in the schist zone and more distributed dextral shear along subvertical foliation planes in the gneiss zone (Fig. 10; e.g. Gasser et al., 2011; Pavlis and Sisson, 1995, 2003; Scharman et al., 2011, 2012). The orientation of stretching lineations associated with the dextral D_3 shearing varies systematically across- and along-strike of the complex. In the schist and northern gneiss zones of transects 1 and 2, the stretching lineation is mainly subhorizontal (Fig. 2; see also Gasser et al., 2011; Pavlis and Sisson, 1995, 2003; Scharman et al., 2011), allowing for only very limited exhumation during shearing. However, stretching lineations in the migmatitic gneiss zone become progressively steeper both from north to south and from west to east (Figs. 2, 10a; Gasser et al., 2011). In transect 2, steep down-dip ductile stretching lineations coincide with the records of the highest pressures (8–11 kbar; Figs. 2, 6). In other words: the steeper the ductile stretching lineation, the higher the exhumation component during ductile shearing (Fig. 10a). We suggest, therefore, that the higher pressure estimates in the southern part of transect 2 associated with the steeper orientation of the stretching lineations in these areas are directly related to higher exhumation values during D_3.

In transect 3, migmatitic gneisses are bounded by different faults (Fig. 2) and stretching lineations plunge to the northwest in the southwestern part of the transect, and to the southeast in the northeastern part of the transect (Figs. 2, 10b; Gasser et al., 2011). Therefore, similarly to transect 2, the rocks within transect 3 probably exhumed during dextral transpression along the bounding shear zones which resulted in considerable exhumation of the gneisses (Fig. 10b).

In addition to the plunging ductile stretching lineations, our structural investigations in transects 1 and 2 revealed the presence of various muscovite- and chlorite-bearing syn- to post D_3 shear zones with north-plunging lineations and north-side-up sense of movement (Figs. 2, 10a; Gasser et al., 2011). These younger ductile to brittle shear zones might form part of a larger shear zone system which localised along the southern border of the migmatitic gneiss zone. This area lies along the strike

of the Contact Fault System and is mainly covered by the Bagley Icefield, which may hide such a major structure (Fig. 2).

7.3.2. The role of the metabasite belt

Between the migmatites of the CMC and the Bagley Icefield, these north-dipping reverse faults localised along the contact between the migmatites and the metabasite belt (Fig. 2). This belt, which is present for most of the length of the CMC, has been suggested to be the consequence of the subduction of a high topographic relief on the downgoing oceanic plate (either a ridge or an intra-oceanic island arc; Bruand et al., 2011; Lull and Plafker, 1990). A study based on sandbox experiments (Dominguez et al., 2000) modelled the subduction of a topographic relief under an accretionary prism. The results of this experiment resemble the geometry of the Chugach accretionary prism: a first accretionary prism (Chugach terrane) is separated by the metabasite belt from a second accretionary prism (Prince William terrane, Fig. 1b). In transect 2, *P–T* estimates from the metabasite belt presented in Bruand et al. (2011) reveal that the *P* estimates from the metabasites from transect 2 (~5 kbar) are considerably lower than the *P* estimates from the northern adjacent migmatites (~11 kbar, Fig. 6). When the topographic high relief is subducted perpendicular to the margin, this is exactly what is observed in the sandbox model, in which the metabasite suture is less exhumed than the accretionary prism behind. The similarities between sandbox experiments and the structure of the Alaskan accretionary prism suggest that the metabasite belt might have played an important role in controlling the pattern of exhumation.

In summary, the new *P–T* data, together with previously published structural data indicate the following exhumation history for the CMC (Fig. 10). Exhumation probably occurred within an overall transpressive regime (Gasser et al., 2011; Scharman and Pavlis, 2012; Scharman et al., 2012), with the resulting strain partitioned between the strike-slip BRF in the north, transpressive shear zones within the western and northern parts of the CMC, and the subvertical D_3 strain zones and the north-dipping reverse faults in the south. This focussed exhumation must have been accompanied by major erosion, which is indicated by sedimentary basins containing Early Eocene detritus from the Chugach terrane farther west of the complex (e.g. Little and Naeser, 1989). The metabasite belt might have served as a localization feature for the high D_3 strain zones in the migmatites and the reverse faults along its southern boundary. The subduction and accretion of this metabasite belt probably acted as a rigid block imposing the transpressive stress field inside the CMC and therewith exhuming the rocks with weaker rheologies. Finally, following the rapid exhumation of the CMC (Gasser et al., 2011; Sisson et al., 1989; Fig. 10), a second terrane accreted (the Prince William terrane) and the metabasite belt acted as a suture between the Chugach and the Prince William terranes.

8. Conclusions

The petrological data presented in this study shed additional light on the uncommon presence of the HT Chugach Metamorphic Complex within the accretionary prism of the southern margin of Alaska in an ongoing subduction setting. The petrology of the CMC is described along three transects crossing the complex and reveals that distinct metamorphic peak parageneses can be recognised: from bt–pl–qz–grt–sil +/− ms or bt–pl–qz–and–ms–chl in the northern schist zone toward liq–bt–pl–qz–grt +/− sil +/− ms in the southern migmatite zone. *P–T* results reveal the following metamorphic conditions and gradients. In the west (transect 1), the conditions increase smoothly from ~550 °C in the northern phyllites via ~600–650 °C in the schist zone to ~650–750 °C in the southern migmatite zone. Both schist and migmatite zones have pressures overlapping around 6 kbar. In the central part (transect 2), the metamorphic conditions increase abruptly from ~550–600 °C and 3–6 kbar in the northern schist zone to ~750 °C and 8–11 kbar in the southern migmatite zone. Along the narrow southeastern part of the complex (transect 3), metamorphic conditions of ~650 °C and 8–10 kbar are reached.

Interpreting the metamorphic temperatures and temperature/pressure ratios in terms of a heat source indicates that the highest grade migmatites have almost 'normal' crustal *T*/*P* ratios typically between 65 °C/kbar and 90 °C/kbar. They appear less thermally perturbed than the somewhat lower grade schists that have *T*/*P* ratios of ≥111 °C/kbar. These observations should be considered when further elaborating on existing models which include the subduction of a spreading ridge as a cause for metamorphism within the CMC.

The clear increase in metamorphic pressure towards the southern (transect 2) and south-eastern parts (transect 3) of the complex indicates that focussed exhumation of these parts must have taken place. In combination with structural data, it is suggested that the subduction of a high topographic relief, associated with the accretion of a lithologically different metabasite belt, induced localised D_3 deformation within the migmatitic zone of the complex. The overall transpressive strain regime was partitioned into strike-slip deformation to the north, along the Border Ranges fault system, and variously oblique transpression within the migmatites and along splay faults of the Contact Fault System, which, aided by focussed erosion, led to localised exhumation of the southern parts of the CMC.

Supplementary data to this article can be found online at http://dx.doi.org/10.1016/j.lithos.2013.12.007.

Acknowledgements

The authors wish to thank T. Pavlis, C. Carson and D. Champagnac for their help during the two field seasons and A. Proyer, R. Strachan and D. Bullen for helpful discussions. Sarah Roeske and Mike Brown are thanked for their useful reviews and the editor for his help. Grateful thanks also to F. Zaccharini and H. Mülhans for the help provided with the microprobe analyses. Thanks to our pilot P. Claus for logistics and amazing landings during fieldwork. The project is financed by FWF project P19366-N10.

References

Barr, T.D., Dahlen, F.A., 1989. Brittle frictional mountain building 2. Thermal structure and heat budget. Journal of Geophysical Research 94, 3923–3947.
Berger, A., Burri, T., Alt-Epping, P., Engi, M., 2008. Tectonically controlled fluid flow and water-assisted melting in the middle crust: an example from the Central Alps. Lithos 102, 598–615.
Beyssac, O., Goffé, B., Chopin, C., Rouzaud, J.N., 2002. Raman spectra of carbonaceous material in metasediments: a new geothermometer. Journal of Metamorphic Geology 20, 859–871.
Beyssac, O., Goffé, B., Petitet, J.P., Froigneux, E., Moreau, M., Rouzaud, J.N., 2003. On the characterisation of disordered and heterogeneous carbonaceous materials by raman spectroscopy. Spectrochimica Acta, Part A 59, 2267–2276.
Bol, A.J., Roeske, S.M., 1993. Strike-slip faulting and block rotation along the contact fault system, eastern Prince William Sound, Alaska. Tectonics 12, 49–62.
Bradley, D.C., Haeussler, P.J., Kusky, T.M., 1993. Timing of Early Tertiary ridge subduction in southern Alaska. U.S. Geological Survey Bulletin 2068, 163–177.
Bradley, D., Kusky, T., Miller, R., Dumoulin, J., Nelson, S.W., Karl, S., 2003. Geologic signature of early Tertiary ridge subduction in Alaska. Geological Society of America, Special Paper 371, 19–50.
Brown, M., 1998a. Unpairing metamorphic belts: P–T paths and a tectonic model for the Ryoke Belt, southwest Japan. Journal of Metamorphic Geology 16, 3–22.
Brown, M., 1998b. Ridge-trench interactions and high-*T*–low-*P* metamorphism, with particular reference to the Cretaceous evolution of the Japanese Islands. Geological Society, London, Special Publications 138, 137–169. http://dx.doi.org/10.1144/GSL.SP.1996.138.01.09.
Brown, M., 2002. Plate margin processes and "paired" metamorphic belts in Japan: Comments on "Thermal effects of ridge subduction and its implication for the origin of granitic batholith and paired metamorphic belts" by Iwamori. Earth and Planetary Science Letters 199, 483–492.
Bruand, E., Gasser, D., Bonnand, P., Stuewe, K., 2011. The petrology and geochemistry of a metabasite belt along the southern margin of Alaska. Lithos 127, 282–297.
Bruhn, R.L., Pavlis, T.L., Plafker, G., Serpa, L., 2004. Deformation during terrane accretion in the St. Elias orogen, Alaska. Geological Society of America Bulletin 116, 771–787.
Caddick, M.J., Konopasek, J., Thompson, A.B., 2010. Preservation of garnet growth zoning and duration of prograde metamorphism. Journal of Petrology 51, 2327–2347.

Cesare, B., Marchesi, C., Hermann, J., Gomez-Pugnaire, M.T., 2003. Primary melt inclusions in andalusite from anatectic graphitic metapelites: implications for the Al_2SiO_5 triple point. Geology 31, 573–576.
Chemenda, A.I., Mattauer, M., Malavieille, J., Bokun, A.N., 1995. A mechanism for syn-collisional deep rock exhumation and associated normal faulting: results from physical modelling. Earth and Planetary Science Letters 132, 225–232.
Cloos, M., 1982. Flow melanges—numerical modeling and geologic constraints on their origin in the Franciscan Subduction Complex, California. Geological Society of America Bulletin 93, 330–345.
Coggon, R., Holland, T.J.B., 2002. Mixing properties of phengitic micas and revised garnet–phengite thermobarometers. Journal of Metamorphic Geology 20, 683–696.
Diener, J.F.A., Powell, R., White, R.W., Holland, T.J.B., 2007. A new thermodynamic model for clino- and orthoamphiboles in the system Na_2O–CaO–FeO–MgO–Al_2O_3–SiO_2–H_2O–O. Journal of Metamorphic Geology 25, 631–656.
Dominguez, S., Malavieille, J., Lallemand, S.E., 2000. Deformation of accretionary wedges in response to seamount subduction: insights from Sandbox experiments. Tectonics 19, 183–196.
Dusel-Bacon, C., 1994. Metamorphic history of Alaska. In: Plafker, George, Berg, H.C. (Eds.), The Geology of Alaska: Boulder, Colorado. Geological Society of America, G-1. The Geology of North America, pp. 495–533.Engebretson, D.C., Cox, A., Gordon, R.G., 1985. Relative motions between oceanic and continental plates in the Pacific basin. Geological Society of America, Special Paper 206, 1–59.
Enkelmann, E., Garver, J.I., Pavlis, T.L., 2008. Rapid exhumation of ice-covered rocks of the Chugach-St. Elias orogen, southeast Alaska. Geology 36, 915–918.
Farris, D.W., Paterson, S.R., 2009. Subduction of a segmented ridge along a curved continental margin: variations between the western and eastern Sanak–Baranof belt, southern Alaska. Tectonophysics 464, 100–117.
Gasser, D., Bruand, E., Stüwe, K., Foster, D., Schuster, R., Fügenschuh, B., Pavlis, T., 2011. Formation of a metamorphic complex along an obliquely convergent margin: structural and thermochronological evolution of the Chugach Metamorphic Complex, southern Alaska. Tectonics 30. http://dx.doi.org/10.1029/2010TC002776.
Gasser, D., Rubatto, D., Bruand, E., Stüwe, K., 2012a. Large-scale, short-lived metamorphism, deformation, and magmatism in the Chugach metamorphic complex, southern Alaska: A SHRIMP U–Pb study of zircons. GSA Bulletin 124, 886–905.
Gasser, D., Bruand, E., Rubatto, D., Stüwe, K., 2012b. The behaviour of monazite from greenschist facies phyllites to anatectic gneisses: an example from the Chugach Metamorphic Complex, southern Alaska. Lithos 134–135, 108–122.
Groome, W.G., Torkelson, D.J., 2009. The three-dimensional thermo-mechanical signature of ridge subduction and slab window migration. Tectonophysics 464, 70–83.
Grujic, D., Hollister, L.S., Parrish, R.R., 2002. Himalayan metamorphic sequence as an orogenic channel: insights from Buthan. Earth and Planetary Science Letters 198, 177–191.
Haeussler, P.J., Bradley, D.C., Wells, R.E., Miller, M.L., 2003. Life and death of the Resurrection plate: evidence for its existence and subduction in the northeastern Pacific in Paleocene–Eocene time. Geological Society of America Bulletin 115, 867–880.
Harris, N., 2007. Channel flow and the Himalayan–Tibetan orogen: a critical review. Journal of the Geological Society 164, 511–523.
Harris, N.R., Sisson, V.B., Wright, J.E., Pavlis, T.L., 1996. Evidence of Eocene mafic underplating during forearc intrusive activity, eastern Chugach Mountains, Alaska. Geology 24, 263–266.
Hodges, K.V., 2006. A synthesis of the Channel-Flow-Extrusion hypothesis as developed for the Himalayan–Tibetan orogenic system. In: Law, R.D., Searle, M.P., Godin, L. (Eds.), Channel Flow, Ductile Extrusion and Exhumation in Continental Collision Zones. Geological Society of London Special Publications, 268, pp. 71–90.
Hodges, K.V., Burchfiel, B.C., Royden, L.H., Chen, Z., Liu, Y., 1993. The metamorphic signature of contemporaneous extension and shortening in the central Himalayan orogen: data from the Nyalam transect, southern Tibet. Journal of Metamorphic Geology 11, 721–737.
Hodges, K.V., Parrish, R.R., Searle, M.P., 1996. Tectonic evolution of the central Annapurna Range, Nepalese Himalayas. Tectonics 15, 1264–1291.
Holland, T.J.B., Powell, R., 1998. An internally consistent thermodynamic data set for phases of petrological interest. Journal of Metamorphic Geology 16, 309–343.
Holland, T.J.B., Powell, R., 2003. Activity–composition relations for phases in petrological calculations: an asymmetric multicomponent formulation. Contributions to Mineralogy and Petrology 145, 492–501.
Holland, T.J.B., Baker, J.M., Powell, R., 1998. Mixing properties and activity–composition relationships of chlorites in the system MgO–FeO–Al_2O_3–SiO_2–H_2O. European Journal of Mineralogy 10, 395–406.
Hudson, T., Plafker, G., 1982. Paleogene metamorphism of an accretionary flysch terrane, eastern Gulf of Alaska. Geological Society of America Bulletin 93, 1280–1290.
Hudson, T., Plafker, G., Lanphere, M.A., 1977. Metamorphic rocks of the Yakutat–St. Elias area, south-central Alaska. U.S. Geological Survey Journal of Research 5, 173–184.
Hudson, T., Plafker, G., Peterman, Z.E., 1979. Paleogene anatexis along the Gulf Alaska margin. Geology 7, 573–577.
Indares, A., Martignole, J., 1985. Biotite–garnet geothermometry in granulite-facies rocks: evaluation of equilibrium criteria. Canadian Mineralogist 23, 187–193.
Iwamori, H., 2000. Thermal effects of ridge subduction and its implication for the origin of granitic batholith and paired metamorphic belts. Earth and Planetary Science Letters 181, 131–144.
James, T.S., Hollister, L.S., Morgan, W.J., 1989. Thermal modeling of the Chugach metamorphic complex. Journal of Geophysical Research 94 (B4), 4411–4423.
Kaneko, Y., Miyano, T., 2004. Recalibration of mutually consistent garnet–biotite and garnet–cordierite geothermometers. Lithos 73, 255–269.
Kaneko, Y., Miyano, T., 2006. Erratum to "Recalibration of mutually consistent garnet–biotite and garnet–cordierite geothermometers". Lithos 86, 347.
Kohn, M.J., Spear, F.S., 2000. Retrograde net transfer reaction insurance for *P–T* estimates. Geology 28, 1127–1130.
Little, T.A., Naeser, C.W., 1989. Tertiary tectonics of the Border Ranges fault system, Chugach Mountains, Alaska: Deformation and uplift in a forearc setting. Journal of Geophysical Research 94, 4333–4359.
Lull, J.S., Plafker, G., 1990. Geochemistry and paleotectonic implications of metabasaltic rocks in the Valdez Group, Southern Alaska. In: Dover, J.H., Galloway, J.P. (Eds.), Geological Studies in Alaska by the U.S. Geological Survey, 1989. U.S. Geological Survey Bulletin, 1946, pp. 29–38.
Mahar, E.M., Baker, J.M., Powell, R., Holland, T.J.B., Howell, N., 1997. The effect of Mn on mineral stability in metapelites. Journal of Metamorphic Geology 15, 233–238.
Marshak, R.S., Karig, D.E., 1977. Triple junctions as a cause for anomalously near-trench igneous activity between the trench and volcanic arc. Geology 5, 233–236.
Maruyama, S., Liou, J.G., Terabayashi, M., 1996. Blueschists and eclogites of the world and their exhumation. International Geology Review 38, 485–594.
Northrup, C.L., 1996. Structural expressions and tectonic implications of general non-coaxial flow in the mid-crust of a collisional orogen: The northern Scandinavian Caledonides. Tectonics 15, 490–505.
Pattison, D.R.M., 1992. Stability of andalusite and sillimanite and the Al_2SiO_5 triple point: constraints from the Ballachulish aureole. Scotland Journal of Geology 100, 423–446.
Pattison, D.R.M., Harte, B., 1988. Evolution of structurally contrasting anatectic migmatites in the 3-kbar Ballachulish aureole, Scotland. Journal of Metamorphic Geology 6, 475–494.
Pavlis, T.L., Roeske, S.M., 2007. The Border Range Fault System, southern Alaska. In: Ridgway, K., Trop, J., Glen, J., O'Neill, J. (Eds.), Geological Society of America Special Paper, 431, pp. 95–128.
Pavlis, T.L., Sisson, V.B., 1995. Structural history of the Chugach metamorphic complex in the Tana River region, eastern Alaska: a record of Eocene ridge subduction. GSA Bulletin 107, 1333–1355.
Pavlis, T.L., Sisson, V.B., 2003. Development of a subhorizontal decoupling horizon in a transpressional system, Chugach metamorphic complex, Alaska: Evidence for rheological stratification of the crust. In: Sisson, V.B., Roeske, S.M., Pavlis, T.L. (Eds.), Geology of a transpressional orogen developed during ridge–trench interaction along the North Pacific margin. Geological Society of America Special Paper, 371, pp. 191–216.
Plafker, G., Moore, J.C., Winkler, G.R., 1994. Geology of the southern Alaska margin: the Geology of North America, G-1. The Geology of Alaska. The Geological Society of America 12, 389–449.
Powell, R., Holland, T., 1988. An internally consistent dataset with uncertainties and correlations: 3. Applications to geobarometry, worked examples and a computer program. Journal of Metamorphic Geology 6, 173–204.
Powell, R., Holland, T., 1994. Optimal geothermometry and geobarometry. American Mineralogist 79, 120–133.
Powell, R., Holland, T.J.B., 1999. Relating formulations of the thermodynamics of mineral solid solutions: activity modelling of pyroxenes, amphiboles and micas. American Mineralogist 84, 1–14.
Sample, J.C., Reid, M.R., 2003. Large-scale, latest Cretaceous uplift along the northeast Pacific Rim: evidence from sediment volume, sandstone petrography, and Nd isotopic signatures of the Kodiak Formation, Kodiak Islands, Alaska. In: Sisson, V.B., Roeske, S.M., Pavlis, T.L. (Eds.), Geology of a transpressional orogen developed during ridge–trench interaction along the North Pacific margin. Geological Society of America Special Paper, 371, pp. 51–70.
Sawyer, E., 2010. Migmatites formed by water-fluxed partial melting of a leucogranite protolith: microstructures in the residual rocks and source of fluid. Lithos 116, 273–286.
Scharman, M., Pavlis, T.L., 2012. Kinematics of the Chugach metamorphic complex, southern Alaska: Plate geometry in the north Pacific margin during the Late Cretaceous to Eocene. Tectonics 31, TC4014. http://dx.doi.org/10.1029/2011TC003034.
Scharman, M., Pavlis, T.L., Day, E.M., O'Driscoll, L.J., 2011. Deformation and structure in the Chugach metamorphic complex, southern Alaska: crustal architecture of a transpressional system from a down plunge section. Geosphere 7, 992–1012.
Scharman, M., Pavlis, T.L., Ruppert, N., 2012. Crustal stabilization through the process of ridge subduction: examples from the Chugach Metamorphic Complex, southern Alaska. Earth and Planetary Science Letters 329–330, 122–132.
Shaw, D.M., 1956. Geochemistry of politic rocks. PartIII: major elements and general geochemistry. Bulletin of the Geological Society of America 67, 919–934.
Sisson, V.B., Hollister, L.S., 1988. Low-pressure facies series metamorphism in an accretionary sedimentary prism, southern Alaska. Geology 16, 358–361.
Sisson, V.B., Pavlis, T.L., 1993. Geologic consequences of plate reorganization: an example from Eocene southern Alaska fore arc. Geology 21, 913–916.
Sisson, V.B., Hollister, L.S., Onstott, T.C., 1989. Petrologic and age constraints on the origin of a low-pressure/high-temperature metamorphic complex, Southern Alaska. Journal of Geophysical Research 94, 4392–4410.
Sisson, V.B., Poole, P.R., Harris, N.R., Burner, H.C., Pavlis, T.L., Copeland, P., Donelick, R.A., McLelland, W.C., 2003. Geochemical and geochronologic constraints for the genesis of tonalite–trondhjemite suite and associated mafic intrusive rocks in the eastern Chugach Mountains, Alaska: a record of ridge-transform subduction: geology of a transpressional orogen developed during ridge–trench interaction along the North Pacific Margin. Geological Society of America, Special Paper 371, 293–326.
Tetreault, J.L., Buiter, S.J.H., 2012. Geodynamic models of terrane accretion: testing the fate of island arcs, oceanic plateaus, and continental fragments in subduction zones. Journal of Geophysical Research 117. http://dx.doi.org/10.1029/2012JB009316. issn: 0148-0227.
Tracy, R.J., 1982. Compositional zoning and inclusions in metamorphic minerals. In: Ferry, J.M. (Ed.), Characterization of Metamorphism through Mineral Equilibria. reviews in Mineralogy, 10, pp. 355–397.

Tracy, R.J., Robinson, P., Thompson, A.B., 1976. Garnet composition and zoning in the determination of temperature and pressure of metamorphism, Central Massachusetts. American Mineralogist 61, 762–775.
Vannay, J.C., Grasemann, B., 2001. Himalayan inverted metamorphism and synconvergence extension as a consequence of a general extrusion. Geological Magazine 138, 253–276.
Vrolijk, P., 1987. Tectonically driven fluid flow in the Kodiak accretionary complex, Alaska. Geology 15, 466–469.
White, R.W., Powell, R., Holland, T.J.B., 2001. Calculation of partial melting equilibria in the system Na_2O–CaO–K_2O–FeO–MgO–Al_2O_3–SiO_2–H_2O (NCKFMASH). Journal of Metamorphic Geology 19, 139–153.
White, R.W., Pomroy, N.E., Powell, R., 2005. An in-situ metatexite-diatexite transition in upper amphibolite facies rocks from Broken Hill, Australia. Journal of Metamorphic Geology 23, 579–602.
White, R.W., Powell, R., Holland, T.J.B., 2007. Progress relating to calculation of partial melting equilibria for metapelites. Journal of Metamorphic Geology 25, 511–527.
Whitney, D.L., Evans, B.W., 2010. Abbreviation for names of rock-forming minerals. American Mineralogist 95, 185–187.
Wopenka, B., Pasteris, J.D., 1993. Structural characteristic of kerogens to granulite facies graphite: applicability of Raman microprobe spectroscopy. American Mineralogist 78, 533–557.
Wu, C.M., Cheng, B.H., 2006. Valid garnet–biotite (GB) geothermometry and garnet–aluminium silicate–plagioclase–quartz (GASP) geobarometry in metapelitic rocks. Lithos 89, 1–23.
Yardley, B.W.D., 1977. An empirical study of diffusion in garnet. American Mineralogist 62, 793–800.
Yardley, B.W.D., Barber, J.P., 1991. Melting reactions in the Connemara Schists: the role of water infiltration in the formation of amphibolite facies migmatites. American Mineralogist 76, 848–856.
Yin, A., 2006. Cenozoic tectonic evolution of the Himalayan orogen as constrained by along-strike variation of structural geometry, exhumation history, and foreland sedimentation. Earth Science Reviews 76, 1–131.